DESIGN AND SYNTHESIS OF ANTHRACENETETRONE-BASED REDOX-ACTIVE POROUS ORGANIC POLYMER AS A CATHODE MATERIAL FOR ZINC-ION BATTERIES

A Thesis Submitted to the
Graduate School of Engineering and Sciences of
İzmir Institute of Technology
in Partial Fulfillment of the Requirements for the Degree of

MASTER OF SCIENCE

in Chemistry

by
FERİT BEGAR

July 2023
İZMİR

We approve the thesis of **Ferit BEGAR**

Examining Committee Members:

_____
Prof. Dr. Armağan Kinal
Department of Chemistry, Ege University

_____
Assoc. Prof. Dr. Ümit Hakan Yıldız
Department of Chemistry, İzmir Institute of Technology

_____
Assist. Prof. Dr. Onur Büyükçakır
Department of Chemistry, İzmir Institute of Technology

20 July 2023

_____
Assist. Prof. Dr. Onur Büyükçakır
Supervisor, Department of Chemistry
İzmir Institute of Technology

_____   _____
Prof. Dr. Gülşah Şanlı Mohamed   **Prof. Dr. Mehtap EANES**
Head of the Department of Chemistry   Dean of the Graduated School of
                                                                    Engineering and Sciences

ACKNOWLEDGMENTS

ABSTRACT

DESIGN AND SYNTHESIS OF ANTHRACENETETRONE-BASED REDOX-ACTIVE POROUS ORGANIC POLYMER AS A CATHODE MATERIAL FOR ZINC-ION BATTERIES

Aqueous zinc ion batteries (AZIBs) are a new class of energy storage devices with significant potential for large-scale applications. However, developing suitable cathode materials that can efficiently and reversibly accommodate Zn^{2+} ions remains a key obstacle in advancing this technology. Porous organic polymers (POPs) are materials characterized by their interconnected network of pores at the molecular level. These versatile polymers exhibit unique properties such as high surface area, tunable porosity, and diverse functionality. POPs hold great potential for various technological advancements, and recently, they have attracted significant interest in energy storage applications due to their exceptional physical and chemical properties, which endow structural durability and electrochemical superiority.

In this study, we reported the synthesis of a new redox-active quinone-rich porous organic polymer (rPOP) as a cathode material for AZIBs. The highly porous nature of rPOP enables successful Zn^{2+} diffusion into the redox centers. The structural durability of the polymeric materials provides ultra-long cycle life. The cell containing rPOP cathode delivered a discharge capacity of 120 mA h g^{-1} at a current density of 0.1 mA g^{-1}. Most importantly, the rPOP revealed extraordinary cycling stability at 1.0 A g^{-1} for 10000 charge/discharge cycles and at 2.0 A g^{-1} for 30000 charge/discharge cycles with capacity retentions of %95 and %66, respectively. The detailed investigation of the charge storage behavior of rPOP cathode, using ex/in-situ analysis, revealed that H^+ acts as a secondary charge carrier along with the Zn^{2+}, contributing to 17% of the overall capacity. This study demonstrates the effective utilization of POPs as a cathode material for AZIBs, and we believe that it will attract the attention of researchers in the energy storage field.

ÖZET

ÇINKO-İYON BATARYALAR İÇİN KATOT MALZEMESİ OLARAK ANTRASENTETRON-ESASLI REDOKS-AKTİF GÖZENEKLİ ORGANİK POLİMERİN TASARIMI VE SENTEZİ

Sulu çinko iyon piller (SÇİP), büyük ölçekli uygulamalar için önemli potansiyele sahip yeni bir enerji depolama cihazları sınıfıdır. Bununla birlikte, Zn^{2+} iyonlarını verimli ve tersine çevrilebilir şekilde barındırabilen uygun katot malzemelerinin geliştirilmesi, bu teknolojinin ilerlemesinde önemli bir engel olmaya devam etmektedir. Gözenekli organik polimerler (GOP'lar), moleküler düzeyde birbirine bağlı gözenek ağları ile karakterize edilen malzemelerdir. Bu çok yönlü polimerler, yüksek yüzey alanı, ayarlanabilir gözeneklilik ve çeşitli işlevsellik gibi benzersiz özellikler sergiler. GOP'lar yapısal dayanıklılık ve elektrokimyasal üstünlük sağlayan olağanüstü fiziksel ve kimyasal özellikleri nedeniyle enerji depolama uygulamalarında önemli ilgi çekmektedir.

Bu çalışmada, SÇİP'ler için katot malzemesi olarak yeni bir redoks aktif kinon açısından zengin gözenekli organik polimerin (rPOP) sentezini bildirdik. rPOP'un oldukça gözenekli yapısı, redoks merkezlerine başarılı Zn^{2+} difüzyonunu mümkün kılar. Polimerik malzemelerin yapısal dayanıklılığı, ultra uzun çevrim ömrü sağlar. rPOP katodunu içeren hücre, 0.1 mA g^{-1} akım yoğunluğunda 120 mA h g^{-1} deşarj kapasitesi verdi. En önemlisi, rPOP, sırasıyla %95 ve %66 kapasite korumalarıyla 1.0 A g^{-1} de 10 000 şarj/deşarj döngüsü için ve 2.0 A g^{-1} de 30 000 şarj/deşarj döngüsü için olağanüstü döngü kararlılığı ortaya koydu. Ex/in-situ analizi kullanılarak rPOP katodunun yük depolama davranışının ayrıntılı araştırması, $H^{+'}$nın Zn^{2+} ile birlikte ikincil yük taşıyıcısı olarak davrandığını ve genel kapasitenin %17'sine katkıda bulunduğunu ortaya çıkardı. Bu çalışma, GOP'ların AZIB'ler için bir katot malzemesi olarak etkin bir şekilde kullanıldığını göstermektedir ve enerji depolama alanındaki araştırmacıların ilgisini çekeceğine inanıyoruz.

TABLE OF CONTENTS

LIST OF FIGURES

LIST OF ABBREVIATIONS

AZIBs	Aqueous Zinc-ion Batteries
LIBs	Lithium-ion Batteries
^{1}H	Proton Nuclear Magnetic Resonance Spectroscopy
CV	Cyclic Voltammetry
GCD	Galvanostatic Charge and Discharge Measurements
^{13}C	Carbon Nuclear Magnetic Resonance Spectroscopy
FTIR	Fourier- Transform Infrared Spectroscopy
CAN	Cerium Ammonium Nitrate
DMF	N,N'-Dimethylformamide
NMR	Nuclear Magnetic Resonance
SEM	Scanning Electron Microscopy
TGA	Thermogravimetric Analysis
PXRD	Powder X-ray Diffraction Analysis
XPS	X-ray Photoelectron Spectroscopy
EtOH	Ethanol
CH$_3$CN	Acetonitrile
BET	Brunauer-Emmett-Teller
MeOH	Methanol
CDCl$_3$	Deuterated chloroform
IUPAC	International Union of Pure and Applied Chemistry
DCM	Dichloromethane
DMSO-d6	Deuterated dimethyl sulfoxide
THF	Tetrahydrofuran
s	Singlet
d	Doublet
t	Triplet
m	Multiplet
dd	Doublet of Doublet

CHAPTER 1

INTRODUCTION

1.1. An Overview of the Design of Organic Cathode Material for Aqueous Zinc-ion Batteries (AZIBs)

The demand for high-performance, environmentally friendly, and low-cost energy storage systems has been growing rapidly in recent years, driven by several factors, including the increasing use of portable devices and efficient utilization of excess energy from renewable energy sources such as solar and wind power.[1] With rapid advancements in portable devices over the last two decades and the availability of more renewable energy sources, energy storage systems are becoming increasingly vital for balancing supply and demand. Energy storage systems allow excess energy generated during times of high production to be stored and used when demand is higher than supply, thus helping to stabilize the grid and reduce the need for expensive peaker plants.[2] Furthermore, energy storage systems are being used to power electric vehicles by allowing them to store and transfer energy without the need for a stationary energy source, which has boosted their growing popularity.[3] Overall, the need for energy storage systems is predicted to accelerate in the following years because of the increasing dependence on portable devices, the efficient use of renewable energy sources, and the necessity for grid stability and reliability.

Rechargeable metal-ion batteries are the most recognized energy storage devices in the energy storage field due to their high energy and power densities with improved cycling stabilities.[4] Lithium-ion batteries (LIBs) have dominated the rechargeable metal-ion battery field due to their high energy density, lightweight, and high rate performance.[5,6] However, their use in large-scale applications is restricted due to the safety concerns arising from using flammable organic solvent as an electrolyte solution, high cost, and low abundance of lithium element.[7] Therefore, the drawbacks encountered in lithium-ion batteries have necessitated the development of alternative metal ion batteries to overcome the limitations of lithium-ion batteries.[8,9] At this point, AZIBs have gained significant interest due to the abundance of Zn metal, which helps reduce costs.

Substituting organic solvents with water-based solutions offers a safer operational environment and makes the batteries more environmentally friendly. Additionally, AZIBs exhibit a high theoretical capacity up to 820 mAh g^{-1} and low redox potential (-0.76 V vs. standard hydrogen electrode), surpassing other mono- and divalent ions (Li$^+$, Na$^+$, K$^+$, Mg^{+2}, Ca^{2+}, and Al^{+3}).[10-13] Despite these superior properties, the lack of cathode materials has impeded their advancement and large-scale applications owing to low capacity, and poor cycling stability. The high polarity of Zn^{2+} ion allows for greater electrostatic interactions with cathode hosts than monovalent cations like Li$^+$, resulting in a substantially slower diffusion rate. Also, the limited working voltage window of AZIBs due to the reduction potential of water limits their energy density. Therefore, it is essential to develop a suitable cathode material that reversibly accommodates Zn^{2+}, has an improved charge storage capability and a long cycle life to advance AZIBs.[14-16] Until now, researchers have explored different types of inorganic cathode materials for use in AZIBs.[17-21] However, these materials have encountered challenges such as gradual loss of capacity and cycling instability. These issues arise from their tendency to dissolve in the electrolyte solution, significant changes in volume, and unstable phase transitions. Also, the toxic nature of these materials, accompanied by their high cost retarded their development in large-scale applications. Recently, organic molecules have been proposed as cathode materials in AZIBs due to their environmental friendliness, lightweight, low cost, and structural tunability at the molecular level. Especially, carbonyl (C=O) and imine (C=N) containing compounds have demonstrated outstanding redox activity among other functional groups.[22-29] Unfortunately, leakage of their discharged products into the electrolyte solution and their weak conductivity have affected their cycling stability and rate performance, inevitably hampering their utilization. Although the linearly linking redox-active organic molecules to make a conductive polymer held promise to the solubility and conductivity issues, inevitable polymer aggregation impeded the Zn^{2+} diffusion into the redox centers.[30-32]

On the other hand, porous organic polymers are a new class of porous material formed by covalent attachment of organic monomers to form 2-D or 3-D architectures. This unique class of polymeric structures has permanent porosity, large surface area, and high physical and chemical stabilities.[33] Additionally, their insoluble skeleton mitigates the potential risk of redox-active units leaching into the electrolyte solution during charging/discharging cycles. Structural modification on monomers and/or post-

functionalization of the polymers allows the adjustment of electrochemical performance by embedding various redox-active centers to the polymer's backbone or embedding functional groups that change the redox centers' electronic environment.[34] However, research on POP-based cathode materials in AZIBs are in their early stages and only limited number of examples exist in the literature.[35-44] Although the reported POP-based cathode materials showed promising electrochemical performance such as high charge storage capacity and rate performance in AZIBs, limitations such as their poor long-term cycling stability, low conductivity, and capacitive charge storage behavior necessitate further investigation to take a step forward.

Herein, we present the synthesis of redox active, quinone rich conjugated microporous polymer (rPOP) as a cathode material in AZIBs by utilizing a modified version of Diels-Alder reaction between hexakis(bromomethyl)benzene and 1,4,5,8-anthracenetetrone. The high abundance of carbonyl groups and permanent porosity facilitated the Zn^{2+} and H^+ diffusion and accommodation of ions at the redox centers, while superior physicochemical stability of the rPOP enhanced the battery's cycle life. It delivered a discharged capacity of 120 mAh g^{-1} at a current density of 0.1 A g^{-1} and revealed a unique capacity retention of 95% and 66 % after 1000 and 30000 cycles at the current densities of 1.0 A g^{-1} and 2.0 A g^{-1}, respectively. Additionally, the slope of the charge-discharge plateau in the galvanostatic charge and discharge measurement are close to zero, which is rare in literature and serves a stable voltage output. The confirmation of the Zn^{2+}/H^+ co-insertion/desertion, structural changes during charge/discharge cycles, and charge storage mechanism of the rPOP was clearly demonstrated using (ex)in-situ characterizations. This study unveils the structure and electrochemical performance relationships and highlights the impact of the inherent structural features of POPs on the performance of AZIBs.

1.2. Porous Materials

Porous materials can be defined as those containing channels, cavities, voids, or pores. The term porosity is commonly observed in living systems and our daily lives, such as lungs, wings of butterflies, honeycombs, coral reefs, sponges, bricks, and more. Scientists have been inspired by these fascinating structure-function relations in naturally occurring systems and stimulated by the idea of creating permanently porous materials in

laboratories. Common examples of synthetically designed subclasses of porous materials are silicates, zeolites, activated carbons, and metal-organic frameworks (MOFs). The properties and applications of each material depend on its pore size, surface area, and chemical composition. The pores in these materials are classified into three categories by IUPAC definition based on the size of the pores (Figure 1.1). According to this classification, pores with a 2.0 nm or less diameter are classified as "micro". On the other hand, pores with diameters between 2-50 nm are called "meso" while pores larger than 50 nm in diameter are called "macro".
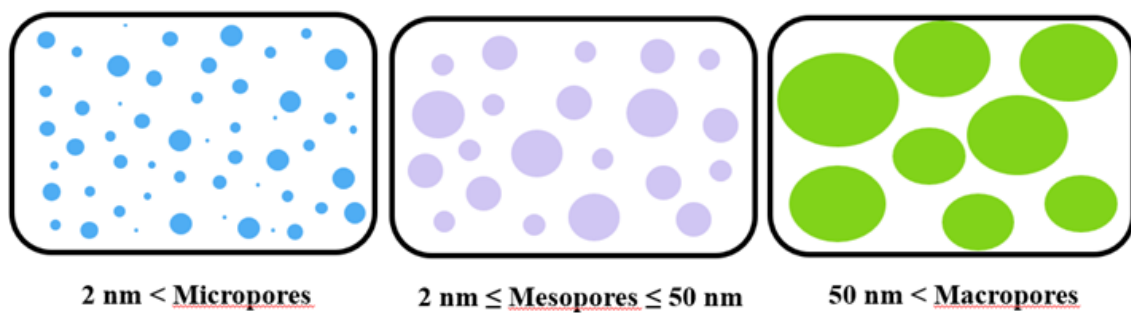
Figure 1.1. Definition of pore sizes according to the IUPAC definition.

The presence of the pores in these materials offers an accessible surface area to the material that can exceed that of a soccer field. The surface areas of porous materials can be measured using gas adsorption analysis. In this method, gas molecules (the most common gas used for this purpose is N_2) at a constant temperature (77 K for N_2) are adsorbed onto the surface of a solid within a range of pressure values. The graph obtained from this technique includes the quantity of adsorbed/desorbed gas (x-axis) versus relative pressure (y-axis) and is called an " adsorption-desorption isotherm". The amount of adsorbed gas at monolayer and multilayer coverage is then used to calculate the surface area using the Langmuir and Brunauer-Emmett-Teller (BET) equations, respectively. Also, isotherms obtained from the adsorption/desorption analysis enable the characterization of pore size and shape.
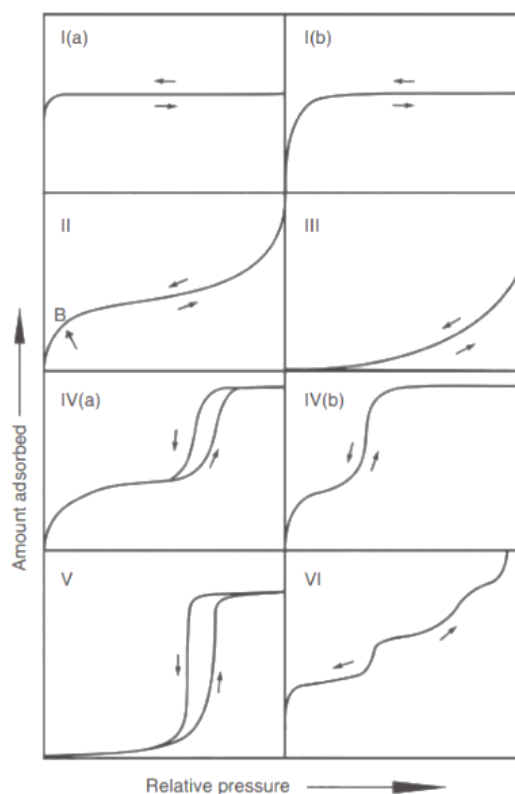
Figure 1.2. Characterization of pore size and shape using isotherms.[Source:45]

Figure 1.2 illustrates six types of isotherms typical for specific pore types and shapes. Type I isotherms are characteristic of microporous solids, especially for MOFs, which show steep uptake at low relative pressure. The micropores are filled, the monolayer is covered during the low-pressure region, and the solid adsorbs no more gas molecules at higher relative pressures. This type of isotherm is divided into two groups type I(a), microporous solids that have mostly narrow pores (≤1 nm), and type I(b), microporous solids with wider micropores along with narrow mesopores (≤2.5 nm). Type II isotherm is attributed to materials with non-porous or microporous materials, whereas type III isotherm describes non-porous or macroporous materials. Mesopores are recognized from type IV isotherms. If the surface of the micro or mesoporous material is hydrophobic, a type V isotherm is commonly observed. Lastly, the type VI isotherm represents a highly homogeneous non-porous structure with layer-by-layer adsorption. The porous nature, high and permanent surface, as well as their diverse chemical composition, facilitate the utilization of porous materials in advanced applications like

gas capture,[46] molecular separations,[47] heterogeneous catalysts,[48] sensing,[49] and drug delivery.[50]

1.3. Porous Organic Polymers (POPs)

Porous organic polymers (POPs) are another class of porous materials constructed by linking organic building units covalently to form 2D or 3D networks. They have attracted colossal interest due to their high porosity, adjustable pore size, high surface area, remarkable physicochemical stability, metal-free skeletons, and structural tunability by modifying monomers and selecting the linkage chemistry. These properties make them promising candidates in various fields, including gas storage and separation, catalysis, sensing, and energy storage systems. The POPs are classified into two categories according to the synthetic strategy employed to create them. The first category includes covalent organic frameworks (COFs) and covalent triazine frameworks (CTFs), which possess long-range order (crystallinity) due to the high reversibility of bond formation, allowing for self-correction to achieve the framework's most thermodynamically favorable state. On the other hand, amorphous porous organic polymers that are constructed using the chemistry offering fast and irreversible bond formation, which facilitates the kinetically controlled polymeric structures, namely conjugated microporous polymers (CMPs), hyper-crosslinked polymers (HCPs), porous aromatic frameworks (PAFs).
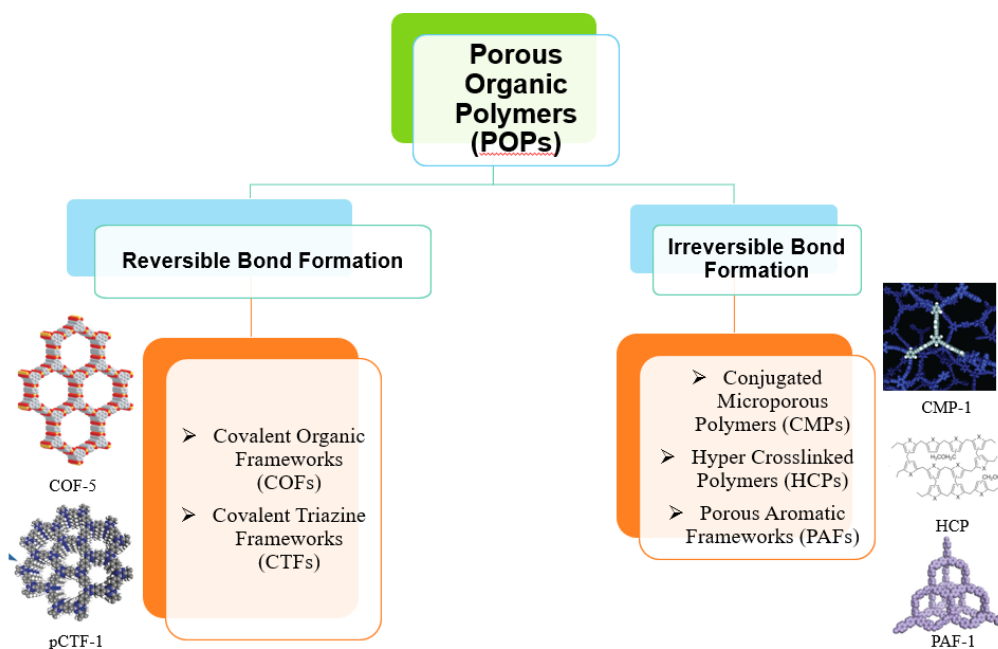
Figure 1.3. Classification of Porous Organic Polymers (POPs).[Source:51]

Various synthesis protocols have been adopted to synthesize POPs: solvothermal, ionothermal, microwave, and mechanochemical. Each method has its pros/cons and must be appropriately selected to synthesize these subclasses of POPs successfully.

1.3.1. Solvothermal Synthesis Method

The solvothermal synthesis methodology is the most common method to prepare POPs. The process is carried out by dissolving the monomers in a carefully chosen solvent system and heating the resulting solution at high temperatures for long hours. The method is comprehensive, which means it can be used to produce all subclasses of POPs. The products of the solvothermal method can be highly crystalline, especially for COFs synthesis, and it is easy to apply this method in the laboratory without the need for expensive equipment. However, the disadvantage of this method is that the reaction times are long, the solvents mixtures contain toxic chemicals, and the reaction yields unprocessable solids, which hinders its potential applications, such as optoelectronic device fabrication. Furthermore, optimizing the reaction parameters for the scale-up is highly difficult.

1.3.1.1. Ionothermal Synthesis Method

The ionothermal reaction involves mixing molten salt or its mixture, which is used as solvent and catalyst, with monomers, and keeping the resulting mixture at elevated temperatures. The reaction conditions are solvent-free, and reaction times are shorter than solvothermal methods. The drawback of this method is that the reactions in this procedure are performed at high temperatures, which causes the decomposition of most of the monomers used in POPs synthesis. This condition limits the selection of the starting materials and constrains the diversity of polymers prepared by following the ionothermal reaction methodology. Additionally, it can be challenging to find a suitable eutectic salt mixture as solvent and catalyst for POPs formation.

1.3.1.2. Microwave-assisted Synthesis Method

In both solvothermal and ionothermal reaction conditions, it is challenging to control the temperature and pressure of the system instantaneously. Microwave method gives this opportunity to control both of parameters. Furthermore, it reduces the reaction time drastically and decreases the amount of by-products within the structure. A related study compared the surface area obtained from COF-5 synthesized from microwave and solvothermal methods, respectively.[51] The resulting COF-5 from the microwave method yielded a higher surface area than the solvothermal method and showed the applicability of this method for COFs synthesis.

1.3.1.3. Mechanochemical Synthesis Method

The POPs can also be prepared by mechanochemical synthesis methodology involving ball milling or simple grinding with a pestle and mortar. The method is easy to operate, rapid, and environmentally friendly due to the elimination of organic solvents (solvothermal method) and inorganic salt (ionothermal method). The first example of mechanochemical synthesis of POPs, particularly a COF, is performed by Banerjee and his co-workers where they have synthesized an imine-linked COFs by mixing and grinding 1,3,5-triformylphloroglucinol with 4-phenylenediamine derivatives.[52] The

formation of COF structure was first realized from the color change (Figure 1.4). Also, facile exfoliation of the COFs layers provides COFs sheets resembling graphene structures.
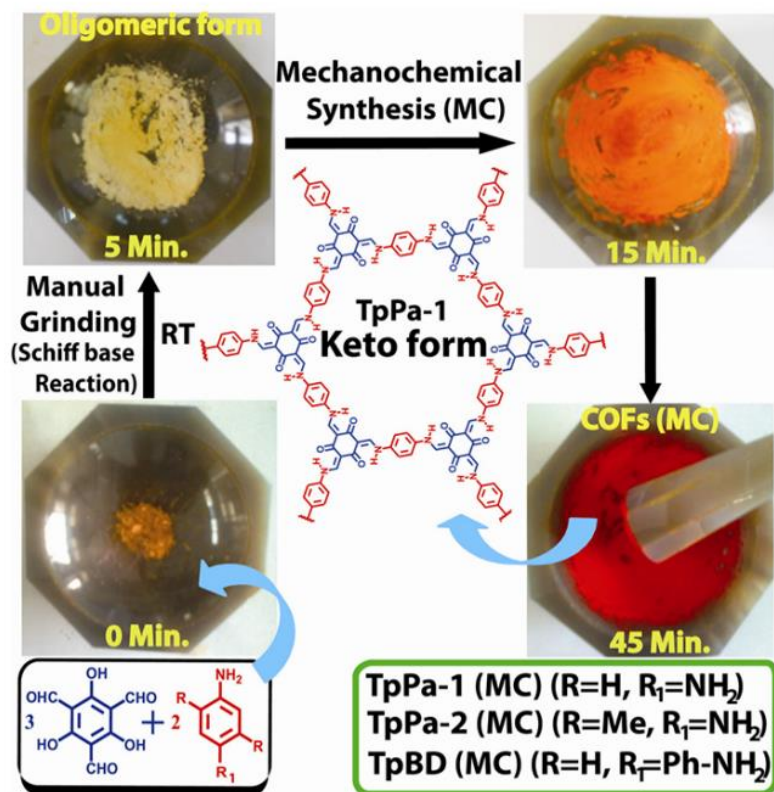
Figure 1.4. Mechanochemical synthesis of TpPa-1 COFs through Schiff base condensation reaction of amines and aldehydes.[Source:52]

1.4 Covalent Organic Frameworks (COFs)

Covalent organic frameworks (COFs), as a subclass of POPs, are porous crystalline polymers composed of light elements such as C, H, N, O, and B. This class of porous polymer exhibit long-range order, permanent porosity, high surface area, and low density. In addition, the size of the pores in COFs can be tuned by increasing the length of the monomer without changing the resulting topology (also called "isoreticular expansion" (Figure 1.5).[53]
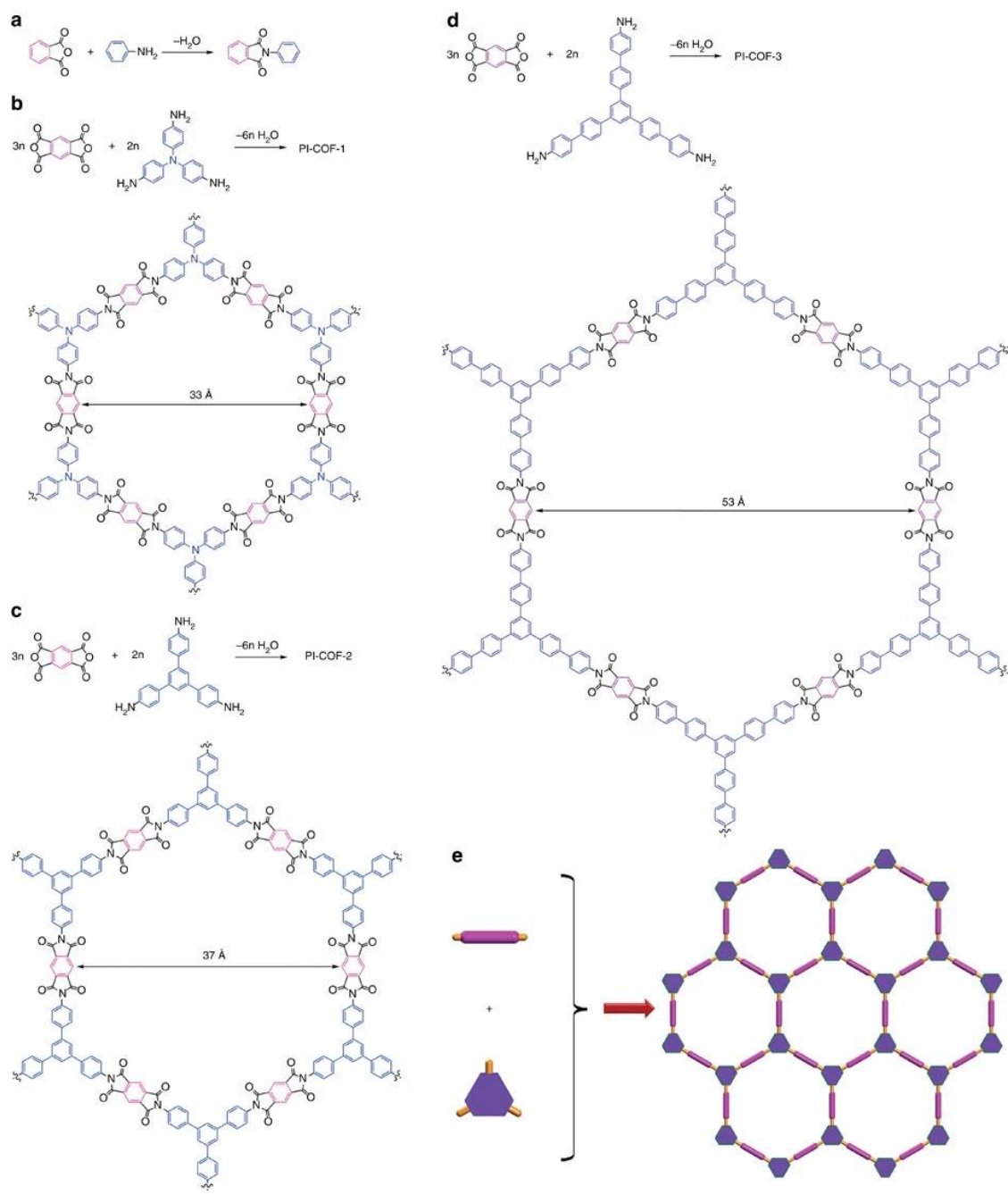
Figure 1.5. a) Synthesis of the model compound that shows the feasibility of polymerization reaction b-d) Variation of pore sizes by changing length of amine linkers e) Representative image of as-prepared PI-COFs structures.[Source:53]

The dimension of the resulting polymer can be pre-organized by the selection of monomers' geometry. If planer molecules are used, then the frameworks adopt 2D networks, whereas using tetrahedral monomers results in 3D structures (Figure 1.6).[54]
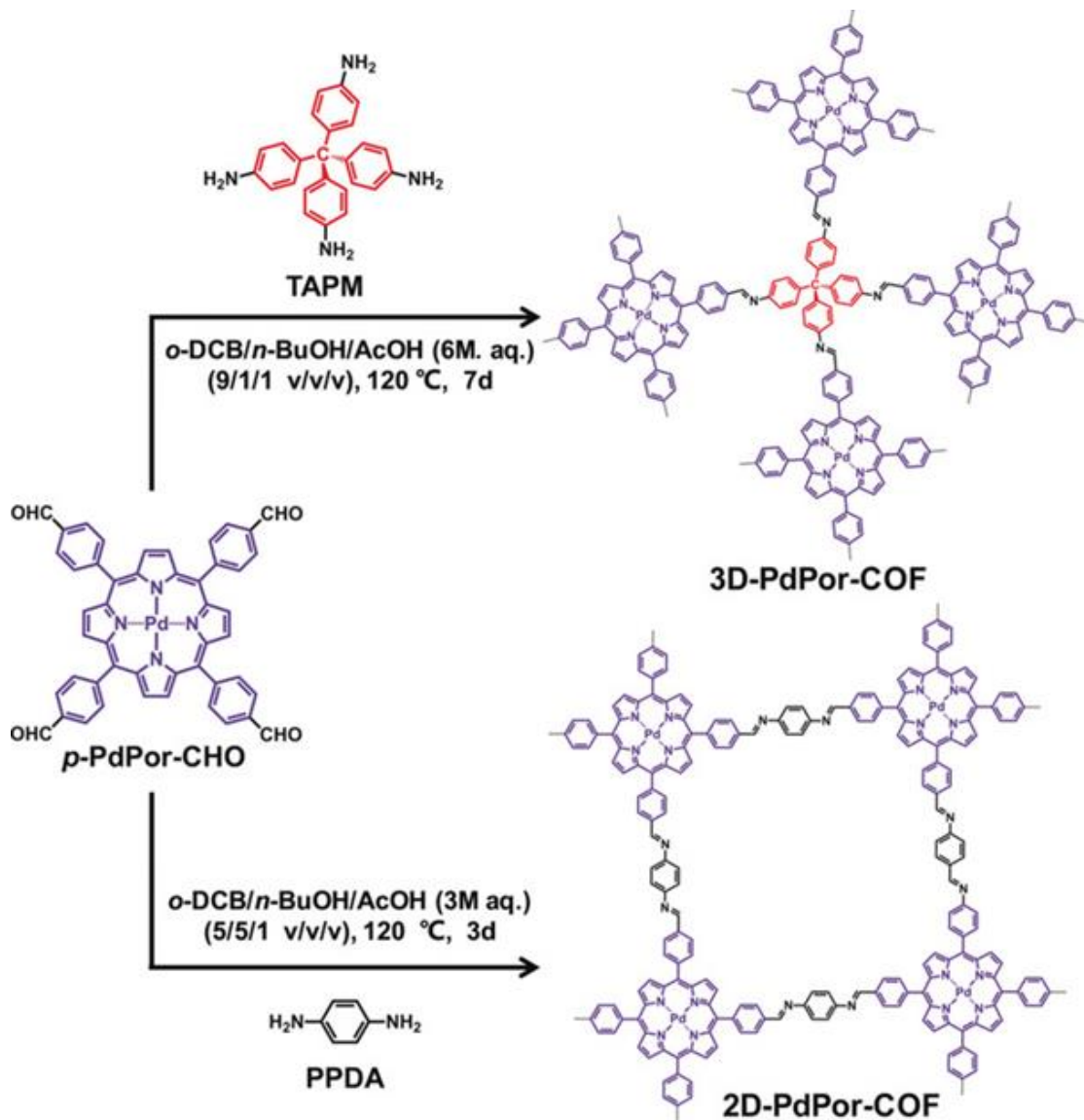
Figure 1.6. Reaction pathways demonstrate the monomer dimension's effect on the resulting COF structures.[(Source:54)]

As depicted in Figure 1.7, reversible bonds such as boroxine, imine, hydrazone, imide, and others are used to construct various crystalline structures. The linkage type used to knit the monomers determines the chemical and physical properties of the resulting polymeric structures.
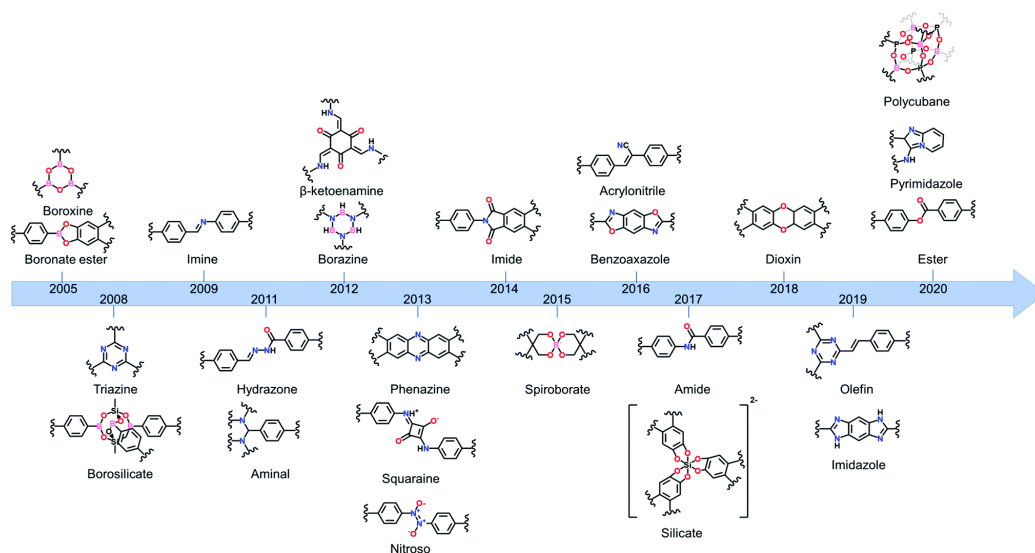
Figure 1.7. Linkage history in the COFs synthesis.[(Source:55)]

For example, boroxine-linked COFs are highly crystalline and thermally stable up to 600 $^{\circ}$C but are susceptible to hydrolysis in water. Imine-linked COFs, synthesized from amines and aldehydes, are also thermally stable, and they show higher hydrostability compared to boron-linked COFs. However, they are still prone to hydrolysis under acidic and basic conditions. In this sense, the linkage chemistry must be selected carefully for the targeted application. The COFs can be synthesized using various methods such as solvothermal, ionothermal, microwave, and mechanochemical.

1.5 Covalent Triazine Frameworks (CTFs)

Covalent Triazine Frameworks (CTFs) are another class of POPs in which the monomers are linked through triazine rings to form crystalline and amorphous polymeric networks. CTFs have attracted significant attention due to their exceptional chemical and thermal stability, high heteroatom content, high surface area, and tunable porosity, making them promising candidates for various applications such as gas storage and conversion, catalysis, and energy storage. The unique properties of CTFs are attributed to the triazine units that form their backbone. These units have a rigid planar structure with a high degree of conjugation, which provides stability to the framework and enables efficient charge transfer. In 2017, Ali Coskun and his co-workers synthesized charged

CTFs through the trimerization of cyano groups under ionothermal reaction conditions (Figure 1.8).[56] They have demonstrated that pore size/volume and surface area can be tuned by differing the amount of $ZnCl_2$ used as both solvent and catalyst for forming cCTFs. Also, the resulting polymers were highly CO_2-philic and could convert the adsorbed CO_2 into cyclic carbonates.
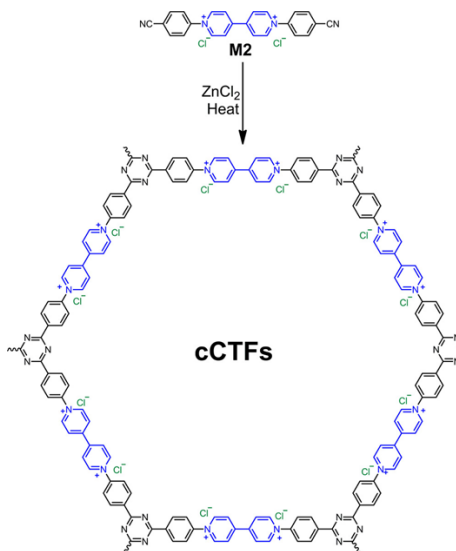
Figure 1.8. Synthesis of charged CTFs by trimerization of 1,1′-bis(4-cyanophenyl)-[4,4′-bipyridine]-1,1′-diium dichloride in the presence of $ZnCl_2$.[Source:56]

CTFs can be synthesized via similar methods as in the case of COFs synthesis, including solvothermal, microwave-assisted, and ionothermal synthesis. The method choice depends on the final product's desired properties and the specific application. Ongoing research is focused on the new chemistry to form triazine rings and increase the diversity of monomers used to design new CTFs.

1.6 Conjugated Microporous Polymers (CMPs)

Conjugated microporous polymer (CMPs) are the most prevalent subclass of POPs formed via fast and irreversible bond formation, thereby lacking long-range order in their structure. They have attracted great interest in recent years due to their unique π-conjugated skeleton with permanent micropores, ease of structural tunability through molecular design, and availability of various feasible synthetic methods such as Suzuki

coupling reaction, Sonogashira-Hagihara reaction, Yamamoto reaction, phenazine ring fusion to link the building units. Due to their intrinsic properties, CMPs show high electrical conductivity, surface area, and thermal stability, making them suitable for various applications, including gas storage, separation, catalysis, and sensing. Also, the porosity can be tailored for specific purposes by regulating the monomers' length and geometry and changing the reaction conditions. For example, in 2008, Cooper and his co-workers demonstrated that the surface area of CMPs synthesized using Sonogashira-Hagihara reaction can be tuned by increasing the length of the linker by producing a series of CMPs, namely CMP-0, CMP-1 CMP-2, CMP-3, CMP-4 and CMP-5 in which the length of the linker used increases from CMP-0 to CMP-5 (Figure 1.9).[57] Their study revealed that increasing the length of the linker decreased the surface area and decreased micropore volume. CMP-0, with the shortest linker distance between the monomers, had a surface area of 1018 m^2g^{-1} with 0.38 cm^3g^{-1} micropore volume. The surface area and micropore volume decrease to 834/0.33 (m^2g^{-1}/cm^3g^{-1}), 634/0.25 (m^2g^{-1}/cm^3g^{-1}), 522/0.18 (m^2g^{-1}/cm^3g^{-1}) and 512/0.16 (m^2g^{-1}/cm^3g^{-1}) from CMP-1 to CMP-5, respectively Also, mesopore contents were increased as the length of the linkers increased.
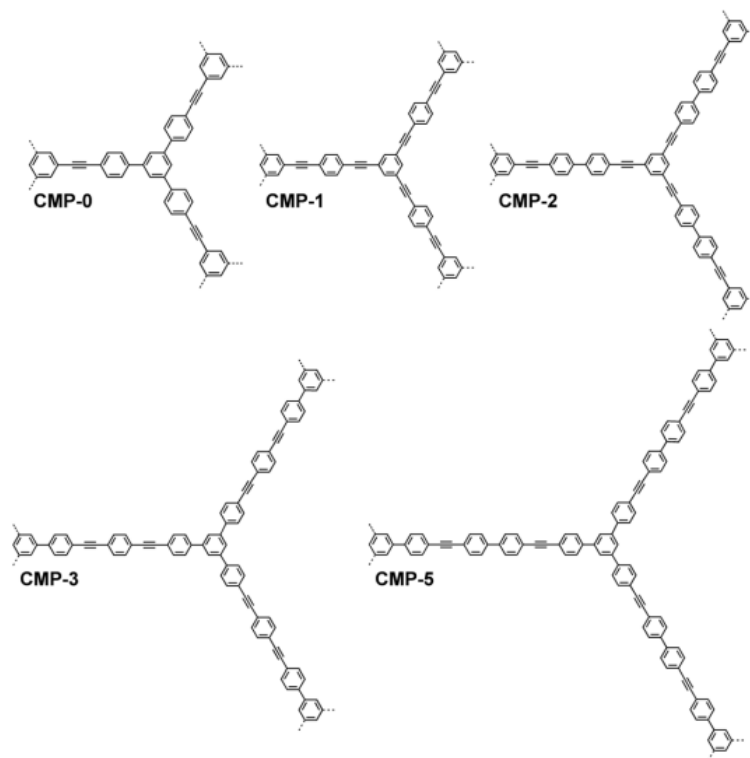
Figure 1.9. Unit cells of CMPs series.[Source:57]

14

The geometry of the reactive groups in monomers also considerably affects the porosity. Arne Thomas, and his co-workers synthesized a series of CMPs namely YSN through self-coupling of 2,2′,7,7′-tetrabromo-9,9′-spirobifluorene, and co-polymerization of 2,2′,7,7′-tetrabromo-9,9′-spirobifluorene with p-dibromo benzene, m-dibromo benzene, o-dibromo benzene, respectively, by Yamamoto coupling reaction (Figure 1.10).[58] The self-coupling of 2,2′,7,7′-tetrabromo-9,9′-spirobifluorene yielded a surface area of 1275 m^2g^{-1}, but it decreased to 887 m^2g^{-1} after copolymerization with p-dibromo benzene. A more pronounced decrease was observed for co-polymerization with m-dibromo benzene which yielded 361 m^2g^{-1} surface area, while a non-porous polymer was obtained with o-dibromo benzene (5 m^2g^{-1}).
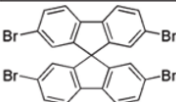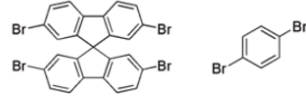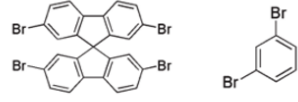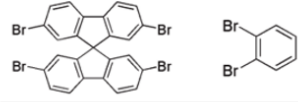
monomers		S_{BET} (m^2/g)	V_{tot} (cm^3/g)	V_{micro} (cm^3/g)
[spirobifluorene tetrabromo structure]		1275	0.997	0.749
[spirobifluorene tetrabromo structure]	[p-dibromo benzene]	887	0.686	0.504
[spirobifluorene tetrabromo structure]	[m-dibromo benzene]	361	0.248	0.179
[spirobifluorene tetrabromo structure]	[o-dibromo benzene]	5	-	-

Figure 1.10. Investigation of self-coupling and copolymerization of 2,2',7,7'-tetrabromo-9,9'-spirobifluorene with dibromo benzene derivatives through Yamamoto coupling reaction and their effect on porosity of the resulting polymer.[Source:58]

1.7 Porous Aromatic Frameworks (PAFs)

Another subclass of POPs is known as porous aromatic frameworks (PAFs), which are prepared covalently attaching aromatic groups using a variety of synthetic approaches such as Sonogashira reactions, Suzuki coupling reactions, Yamamoto reactions, etc. to create amorphous three-dimensional polymeric networks. Besides their

large surface area exceeding 5000 $m^2 g^{-1}$, these architectures have remarkable thermal and chemical stabilities. The first example of PAFs named "PAF-1" was synthesized in 2009 by Zhu and his co-workers through self-coupling of tetrakis(4-bromo-phenyl)methane by nickel(0)-catalyzed Yamamoto-type Ullmann coupling reaction (Figure 1.11).[59]
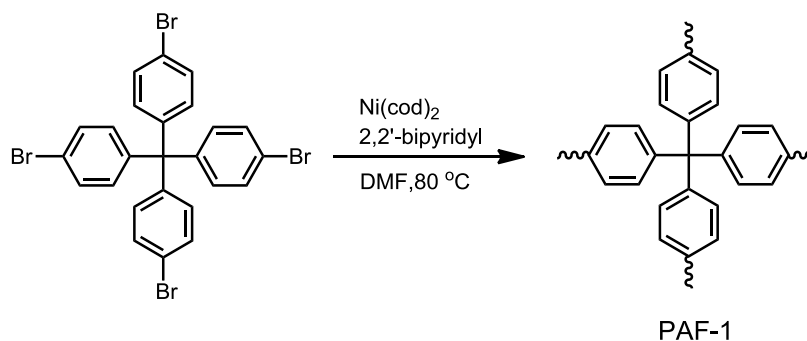
Figure 1.11. Synthesis of PAF-1.[(Source:59)]

The resulting polymer was activated at 200 ^{o}C to remove the solvent molecules, and the N_2 adsorption isotherms are collected at 77 K to investigate the porosity and surface area of the materials. With the presence of both micropores and mesopores, the BET surface area was calculated as 5600 $m^2 g^{-1}$. The TGA analysis showed that the material was stable up to 520 ^{o}C and the PAF-1 retained its structural integrity even after boiling it in water for 7 days. Taking advantages of high surface area and high micropore volumes, the PAF-1 showed high uptake capacities for H_2 and CO_2 gases as well as vapors of benzene and toluene. PAFs are still a relatively new class of materials, and much remains to be discovered about their properties and potential applications. However, the unique combination of high surface area, chemical and thermal stabilities make PAFs a promising class of materials for a wide range of applications in areas such as gas storage, catalysis, and sensing.

1.8 Hyper Cross-linked Polymers (HCP)

Hyper-crosslinked polymers (HCPs) are a class of porous polymers that are formed by crosslinking aromatic monomers through mainly Friedel-Crafts reaction. These polymers have a high degree of crosslinking, resulting in a highly porous structure

16

with a large surface area and tunable pore size. Because of the easy operation and adaptable synthetic technique, a wide range of aromatic monomers can create polymer networks with diverse pore topologies or employ specific functionalities that enhance the high surface area and unique properties. One distinct advantage of HCPs is that the reagents used in the synthesis are highly abundant in chemical markets and thus their synthesis are easy and cheap. Also, the yields of polymerization reactions are high, making HCPs polymers comparable with commercially available porous materials such as zeolites and activated carbons. HCPs have been studied for various applications, including gas storage and separation, catalysis, and environmental remediation. In 2011, Bien Tan's group reported the synthesis of a series of HCPs by knitting rigid aromatic monomers such as benzene, biphenyl, and 1,3,5-triphenylbenzene in the presence of formaldehyde dimethyl acetal as external cross-linker (Figure 1.12).[60] The synthetic method (Friedel-craft) was simple, the yield of reactions was higher than 90%, and methanol was detected as only a by-product. Depending on the monomer selection, the as-synthesized microporous polymers have surface areas between 815-1391 m^2g^{-1}.
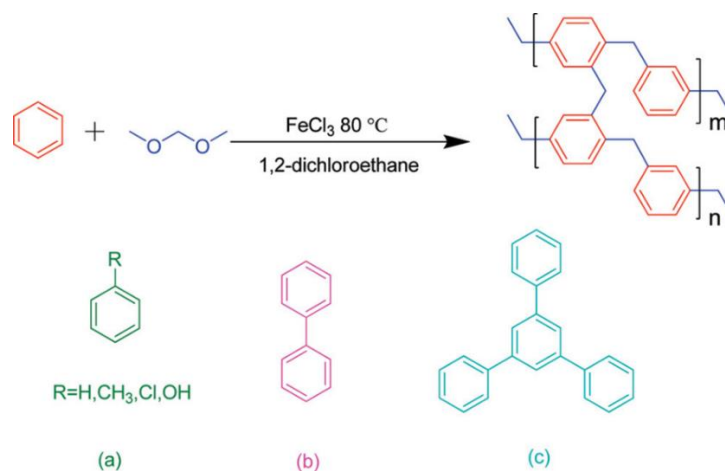
Figure 1.12. Schematic illustration of synthetic route for the synthesis of HCPs where (a),(b) and (c) are the monomers used to create the polymeric network.[Source:60]

The following year, the same group synthesized HCPs from heteroaromatic compounds such as thiophene, pyrrole, and furan under mild reaction conditions using the same external cross-linker (Figure 1.13).[61] Among the obtained polymers, pyrrole-based HCPs showed exceptional CO_2 adsorption capacity with high CO_2/N_2 selectivity.
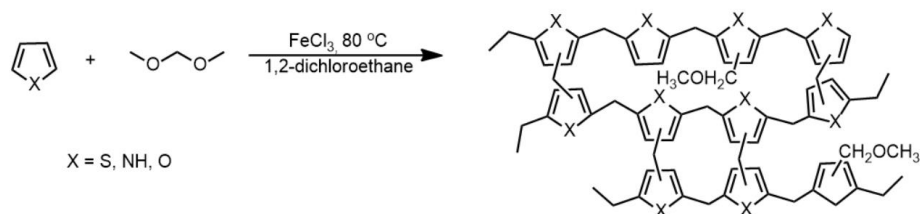
Figure 1.13. Synthesis of heteroaromatic based HCPs via friedal-crafts reactions of thiophene, pyrrole and furan monomers in the presence of an external linker.[Source:61]

1.9 Redox Active POPs as Cathode Material in Zinc Ion Battery

Inherent properties of POPs, such as π-conjugated backbone, rich redox active sites, adjustable pore size, superior physicochemical stability, and high surface area, make them suitable candidates as cathode material in aqueous zinc ion batteries (AZIBs). Also, their insoluble nature in both water and organic solvents eliminates the leaching of redox-active units into the aqueous solution during charge/discharge cycles and improves the long-term cycling stability of the battery. Furthermore, structural modifications on the monomers can be performed to adjust their electrochemical performance. Up to now, most of the subgroups of the POPs, including COFs, CTFs, CMPs and HCPs have been studied as cathode materials in mostly lithium-ion batteries along with sodium and potassium ion batteries. Although POPs have revealed promising electrochemical performance in terms of capacity and long-term stability in rechargeable AZIBs, only a limited number of research studies have been published in the literature, and their detailed investigation on structure/electrochemical performance relations as cathode material in AZIBs is in its early stage. For these reasons, designing new redox-active porous organic polymers with excellent electrochemical performance and understanding the origin of the Zn^{2+} ion storage is critical for developing state-of-art AZIBs.

1.9.1 Working Mechanism of Zinc-ion Battery

A "battery" is a device that stores and converts chemical energy into electrical energy and is made up of one or more electrochemical cells. Each cell contains a negative

electrode (anode), a positive electrode (cathode), a separator, and an electrolyte (Figure 1.14). The anode electrode tends to be oxidized and produces electrons that flow through the cathode electrode, which tends to accept the electrons. The separator prevents direct contact between the electrode and allows for the diffusion of ions during charge and discharge. The electrolyte solution is used for charge balancing. In AZIBs, the anode is zinc metal, filter membranes are the most common separator, and several electrolytes can be prepared using an aqueous solution of $ZnSO_4$, $Zn(CF_3SO_3)_2$, and $ZnCl_2$. Inorganic, organic or inorganic/organic hybrid materials can be used as cathode-active materials. The majority of the active material used to create the cathode is combined with a conductive additive, like carbon black, to improve the electrode's conductivity and a binder to create contact between the active material and conductive additive.
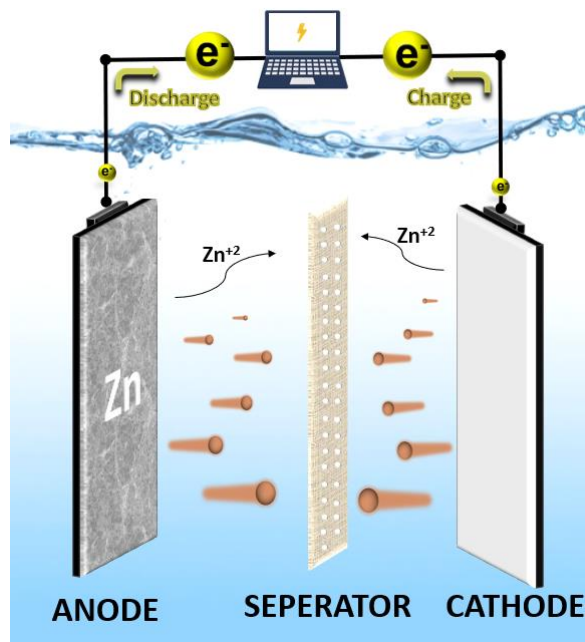
Figure 1.14. Schematic representation and working mechanism of Zinc-ion battery cell.

A battery's primary function is to store and distribute the charge. It does so through discharge/charge cycles. During charging, non-spontaneous reactions are forced to take place by applying an external voltage to the cell, and zinc ions migrate from the cathode to the anode, and electrons flow to the anode part through the current collector. In this way, the charge is stored. During the discharging, the spontaneous reactions occur, and the flow of zinc ions and electrons are reversed. They move from anode to cathode, and

the battery does work during this process. This time, the stored charge is delivered. Accommodation of zinc ions at the cathode can follow several mechanisms such as intercalation, coordination reaction, and conversion reaction, depending on the cathode material used.

1.10 Literature Studies

The first example of POPs as cathode material in AZIBs was published in 2019 by Rahul Banerjees' group.[41] In this study, a COF structure named "HqTp" was synthesized by grinding 2,5-diaminohydroquinone dihydrochloride and 1,3,5-triformylphloroglucinol with p-toluenesulfonic acid as catalyst (Figure 1.15).
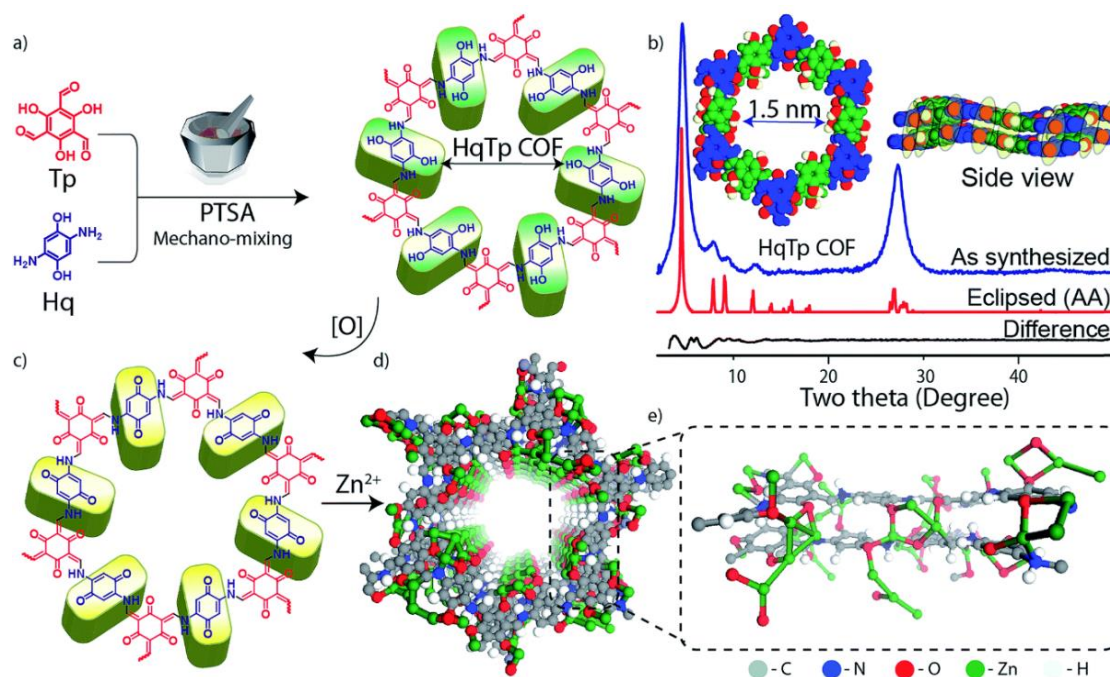
Figure 1.15. (a) Synthetic pathway for the construction of HqTp COF (b) PXRD patterns of simulated and as-synthesized HqTp (c) Oxidation reaction of hdyroquinone to quinone (d) Theoretical model of Zn^{2+} association with COF layers.[Source:41]

The as-synthesized COFs structure was mixed with a conductive additive and a binder to prepare the cathode. Then, the cell was assembled using zinc foil as an anode, aqueous $ZnSO_4$ solution as an electrolyte, nafion membrane as separator, and cathode

material. The galvanostatic charge-discharge (GCD) measurements showed that the cell revealed a discharge capacity of 276.0 mA h g^{-1} at a current density of 0.125 A g^{-1}. To test the long-term cycling stability of HqTp , the cell was cycled 1000 times at a current density of 3.75 A g^{-1} and retention of % 95 of its initial capacity was observed (Figure 1.16. a-b). Several ex-situ analyses were performed to investigate the charge storage mechanism. XPS spectra of the discharge electrode displayed the peaks of Zn^{2+} and the intensity of these peaks has decreased upon charging, confirming reversible insertion/desertion of Zn^{2+}. Also, the discharged electrode was analyzed using FTIR spectroscopy to understand which functional groups in the COFs structure were responsible for charge storage. FTIR spectra of the electrode at pristine, charged and discharged states showed that the carbonyl (C=O) peak has diminished during discharge and the same peak was recovered upon charging. In addition, the solid state ^{13}C NMR spectrum of the discharged electrode showed that the carbon atom of the carbonyl group in the framework has shifted to the downfield by 6 ppm compared to the pristine COFs due to the insertion of Zn^{2+} ions (Figure 1.16 c-d). These results indicated that the carbonyl groups are the active sites for anchoring Zn^{2+} ions.
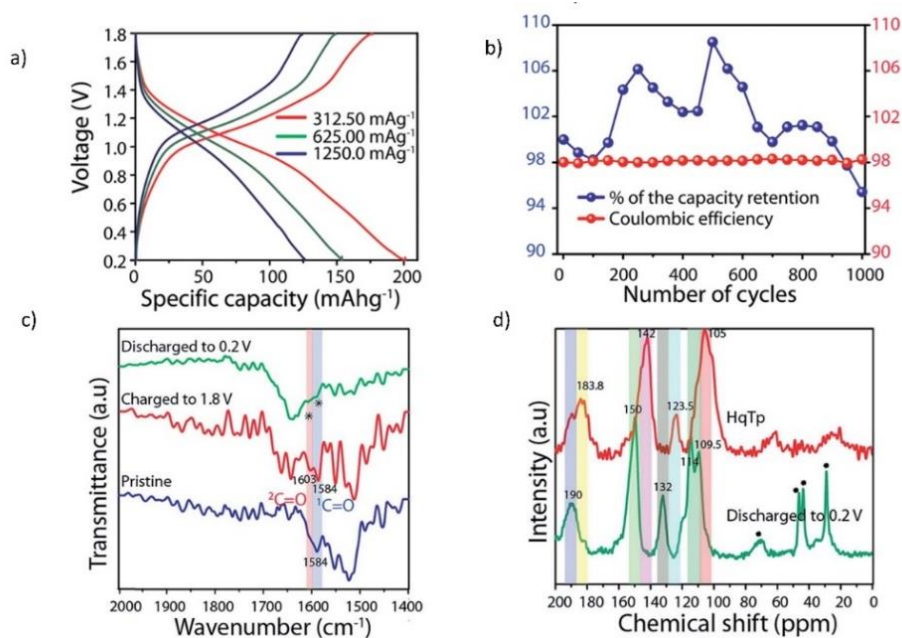
Figure 1.16. (a) Galvanostatic discharge/charge measurements at various current densities (b) Long-term cycling stability test of HqTp electrode (c) FTIR spectra of HqTp electrode at discharge, charged and pristine states (d) Solid-state ^{13}C NMR spectra of HqTp and discharged electrode.[Source:41]

In 2020, Husam N. Alshareef and his co-workers designed a new COFs called "PA-COF" through the solvothermal reaction between hexaketocyclohexane and 2, 3, 7, 8-phenazinetetramine (Figure 1.17).[42] The skeleton of PA-COF features nitrogen-rich phenanthroline groups that are highly electron-rich and can facilitate effective Zn^{2+} infiltration when used as cathode material in zinc-ion supercapatteries.
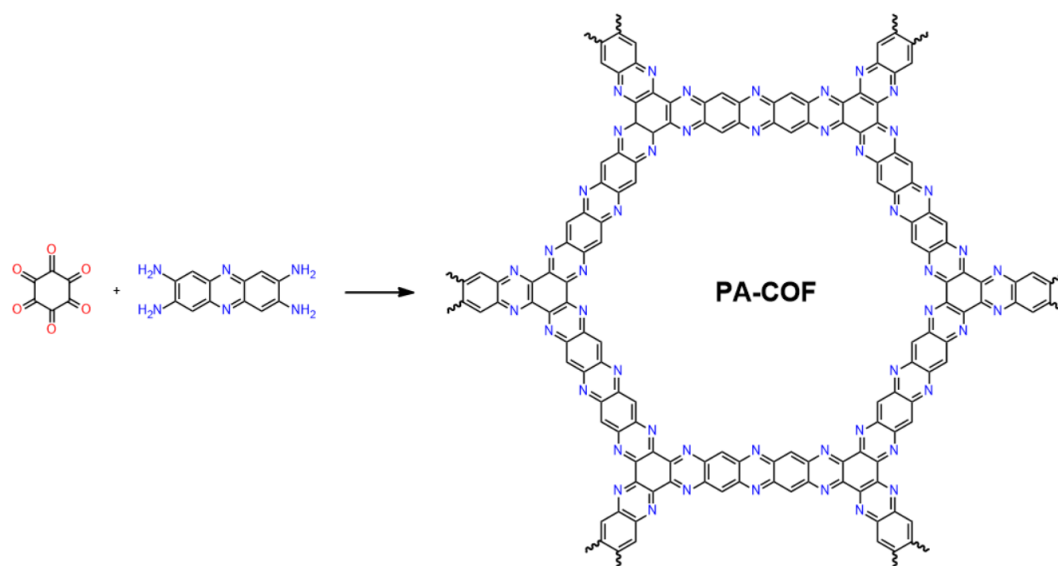
Figure 1.17. Synthesis of PA-COF through condensation reaction of hexaketocyclohexanone and 2,3,7,8-phenazinetetramine.[Source:42]

The as-prepared COFs material was combined with carbon black as a conductive additive and PTFE as a binder to make the cathode. Then, the zinc anode and PA-COF cathode were joined in the presence of 1.0 M $ZnSO_4$ electrolyte, and the electrodes were separated using a glass fiber separator (Figure 1.18 a). From the GCD measurements, the cell demonstrated a capacity value of 247 mA h g^{-1} at a current density of 0.1 A g^{-1} (Figure 1.18. c). The rate performance of the cell was investigated at various current densities. The capacity values of 265, 234, 202, 176, 153, 125, 93, and 68 mA h g^{-1} were recorded when the cell was operated at 0.05, 0.1, 0.2, 0.5, 1.0, 2.0, 5.0, and 10 A g^{-1}, respectively. Also, %90 of the initial capacity was regained when the current density switched back to 0.05 A g^{-1} (Figure 1.18. e). The cycling stability of PA-COF was studied at a current density of 1.0 A g^{-1}. The %99.6 of its initial capacity was retained after 10000 charge/discharge cycles (Figure 1.18. f).
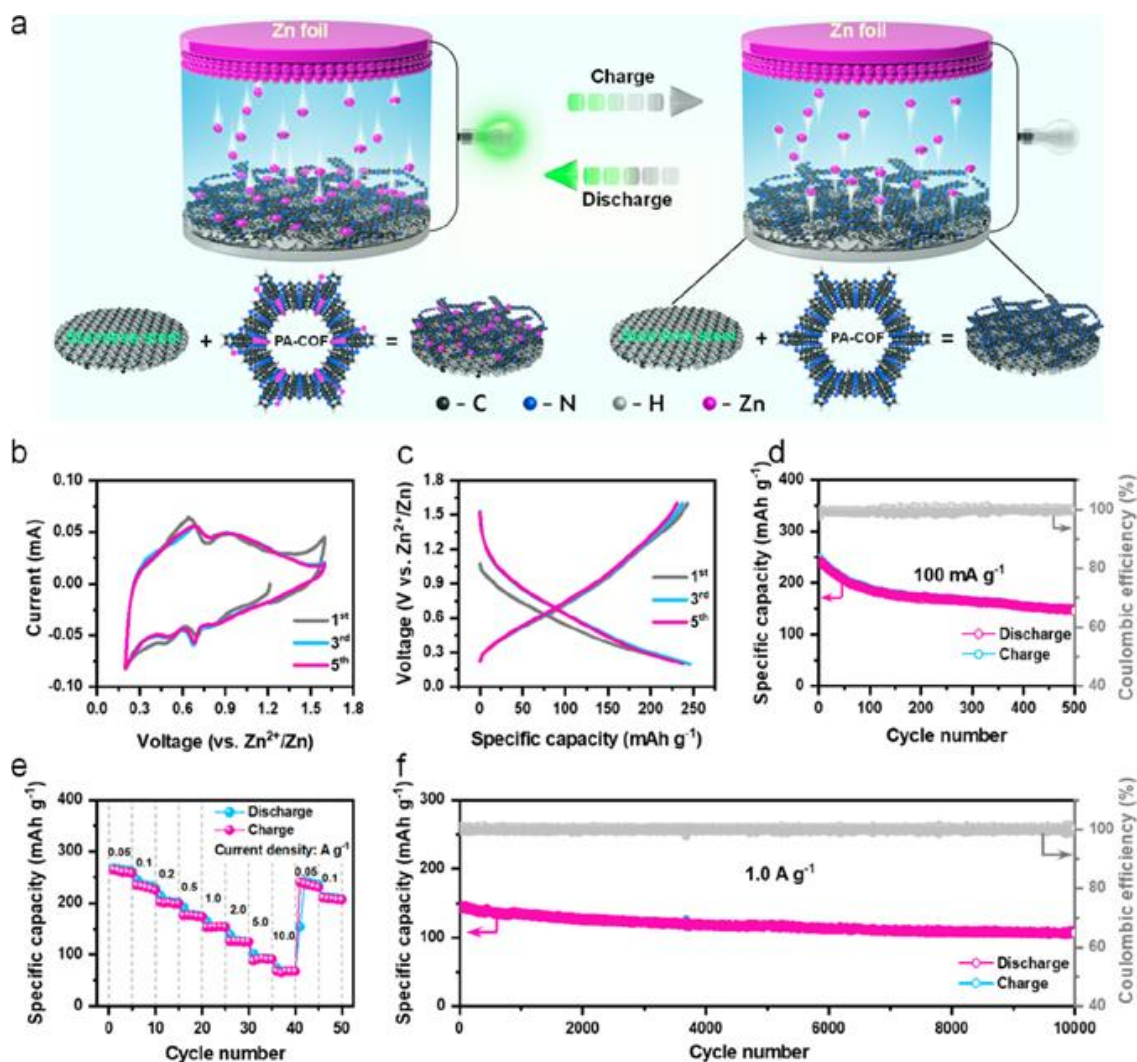
Figure 1.18. (a) Schematic representation of cell incorporating PA-COF during charge and discharge (b) Cyclic voltammetry (CV) curves of PA-COF cathode at a scan rate of 0.05 mV s^{-1} within 0.2-1.6 voltage range (c) GCD at 0.1 A g^{-1}. (d-e) Long-term cycling stability of cathode electrode at different current densities (e) Rate capability test of PA-COF electrode.[Source:42]

The charge storage behavior of the PA-COF was probed using both electrochemical measurements and ex-situ methods. The cell containing PA-COF was cycled in separate electrolyte solutions, including 1.0 M Na$_2$SO$_4$ at pH=7, 1.0 M Na$_2$SO$_4$ at pH=5 and 1.0 M ZnSO$_4$ at pH=7 at the same current density. The results from GCD measurements showed the highest capacity value of 270 mA h g^{-1} with ZnSO$_4$ electrolyte solution, followed by 150 mA h g^{-1} with Na$_2$SO$_4$ at pH=5 and 100 with Na$_2$SO$_4$ at pH=7. Also, the area under the CV curve of ZnSO$_4$ solution was dominantly greater than the others. These comparative results suggest that Zn^{2+} insertion dominated the charge

storage. In addition to the electrochemical analysis, TEM elemental mapping studies showed the emergency of Zn signal after the second discharge and the disappearance of Zn signal after recharge confirms the reversibility of the Zn^{2+} insertion/desertion. To detect the possible H^+ co-insertion with Zn^{2+}, solid-state ^{13}C NMR analysis was performed. A new peak at 3 ppm was evolved after discharging the electrode in D_2O solution. This peak is attributed to D^+ ions in the PA-COF and further proved with additional NMR experiments. Functional groups responsible for charge storage were determined using solid-state ^{13}C NMR and XPS analysis. It was found that C-C=N groups were the active sites for anchoring Zn^{2+}/H^+.

To examine the role of functional groups in the COFs structure and how they affect the electrochemical performance of AZIBs, Alshareef and co-workers prepared two structurally similar COFs materials (HA-COF and HAQ-COF) through the condensation reactions of 1, 2, 4, 5-tetramine benzene and 1,2,4,5-tetramino-benzoquinone with hexaketocyclohexane (Figure 1.19).[43]
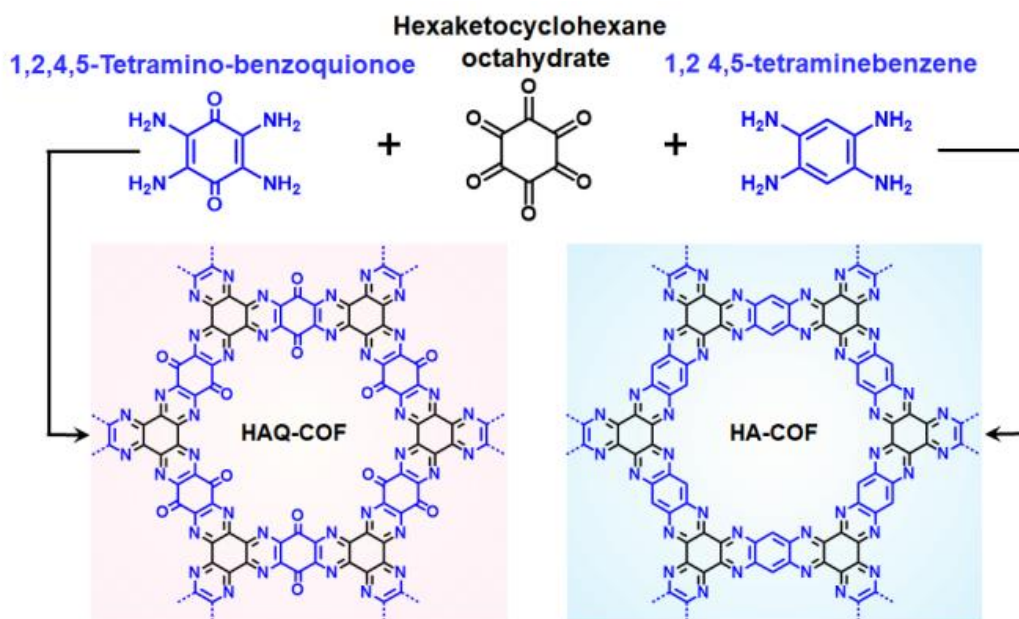
Figure 1.19. Synthesis route of HAQ-COF and HA-COF.[Source:43]

These COFs are well-suited for structure/electrochemical performance evaluation because the highly conjugated and planar skeleton of HA-COF and its quinone functionalized form HAQ-COF enable the study of quinone moieties' effect on

24

electrochemical activity (Figure 1.20 a-b). The performance of the cells assembled from the as-prepared COFs, zinc foil, and 2.0 M ZnSO$_4$ was tested using GCD measurements. The HAQ-COF electrode delivered a discharge capacity of 344 mA h g^{-1} at a current density of 0.1 A g^{-1} which is nearly two times higher than the HA-COF (195 mA h g^{-1}) at the same current density (Figure 1.20. c-e). Additionally, the CV curves of the two electrodes showed that the reduction potential of HAQ-COF was increased compared to the HA-COFs, which is in accordance with the increased capacity of HAQ-COFs. The rate performance of the two electrodes was evaluated at current densities of 0.1, 0.2, 0.5, 1.0, 2.0, 5.0, and 10 A g^{-1}, respectively. The cell containing the HAQ electrode delivered capacities of 339, 317, 279, 255, 228, 170, and 95 mA h g^{-1} while HA-COF delivered nearly half of the capacity obtained from the HAQ-COF at the same current densities. The long-term cycling stability of the electrodes was also compared. HAQ-COF retained %75 of its initial capacity during 10000 cycles at a current density of 5.0 A g^{-1}. On the other hand, HA-COF maintained 69% of its initial capacity after 10000 cycles at the same current density (Figure 1.20. f-g). The electrochemical investigations showed that the HAQ-COF surpassed the HA-COFs and indicated that quinone groups contribute to enhance the charge storage in AZIBs.
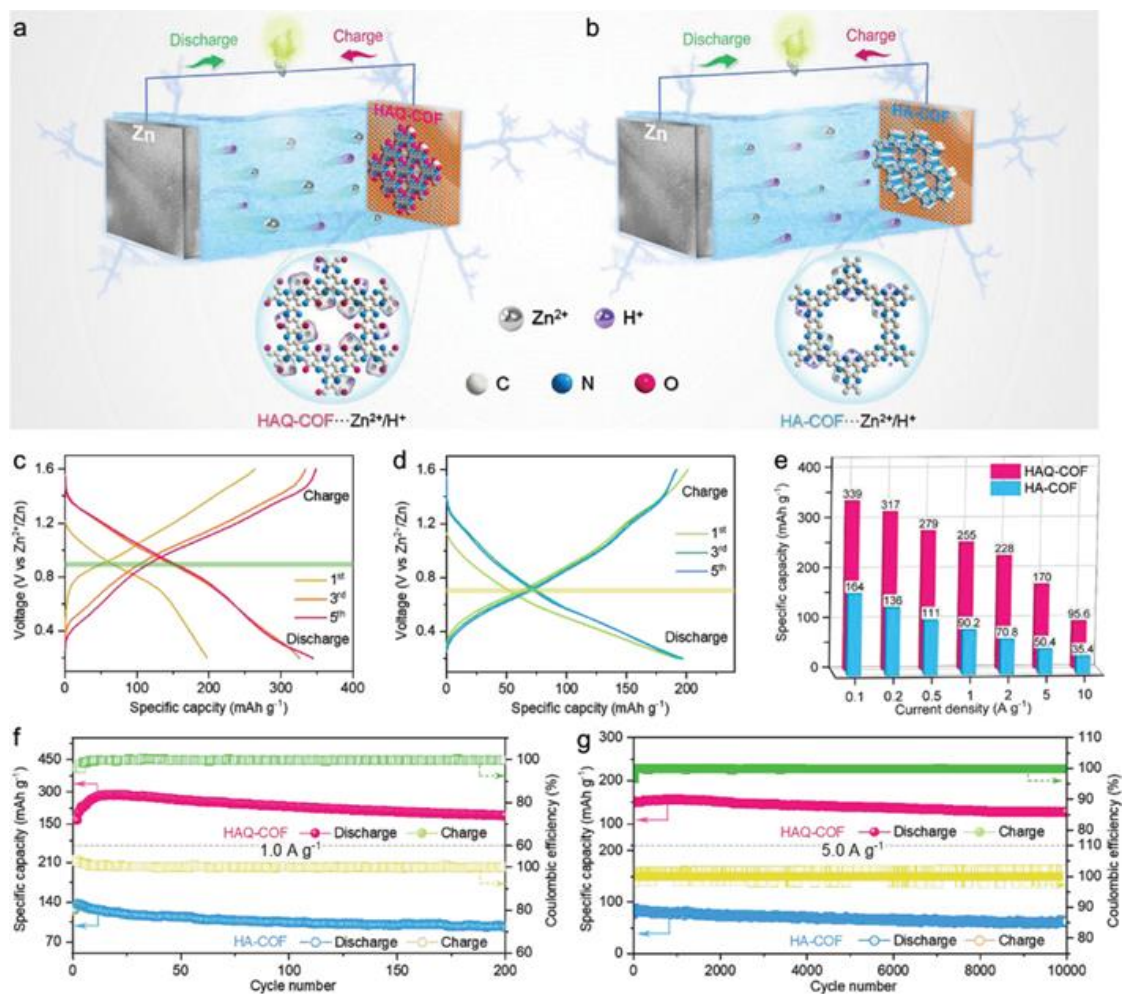
Figure 1.20. (a,b) The cells incorporating HAQ-COF and HA-COF electrodes, respectively (c-d) GCD measurements of HAQ-COF and HA-COF, respectively (e) Rate performance comparison at various current densities (e-f) Long-term cycling stability of the electrodes with coulombic efficiency at 1.0 A g^{-1} for 200 cycles and at 5.0 A g^{-1} for 10 000 cycles, respectively.[Source:43]

To verify the storage mechanism of Zn^{2+} or H^{+} and their co-insertion behavior, electrodes have been tested separately in both aqueous and non-aqueous electrolytes (Note that using non-aqueous electrolytes eliminates the presence of protons in the environment). For this purpose, zinc trifluoromethanesulfonate in water (ZnTFS/H$_2$O) and acetonitrile (ZnTFS/ACN) systems were used as electrolytes. After electrochemical activation within the 30 charge/discharge cycles, both HAQ and HA electrodes revealed elevated discharge capacities with ZnTFS/H$_2$O than ZnTFS/ACN (Figure 1.21). This result demonstrates the contribution of H^{+} to the total capacity. In addition, the Zn^{2+} association of HAQ and HA electrodes were compared. According to the discharge

capacity measured in a non-aqueous system, the HAQ-COF intercalated 0.00197 mM Zn^{2+} while HA-COFs retained 0.000628 mM Zn^{2+}. This result supports the fact that quinone groups strengthen the Zn^{2+} uptake. The increased Zn^{2+} uptake with HAQ electrode was further studied using an aqueous electrolyte system. It was found that the HAQ-COF electrode has a higher Zn^{2+} capacity contribution than the HA-COF electrode, reaching 59.7%, while the Zn^{2+} capacity contribution in the HA-COF maintains at around 43%. It can be concluded that attaching quinone groups also enhance the propensity of electrode materials to coordinate with Zn^{2+} instead of H^{+}.
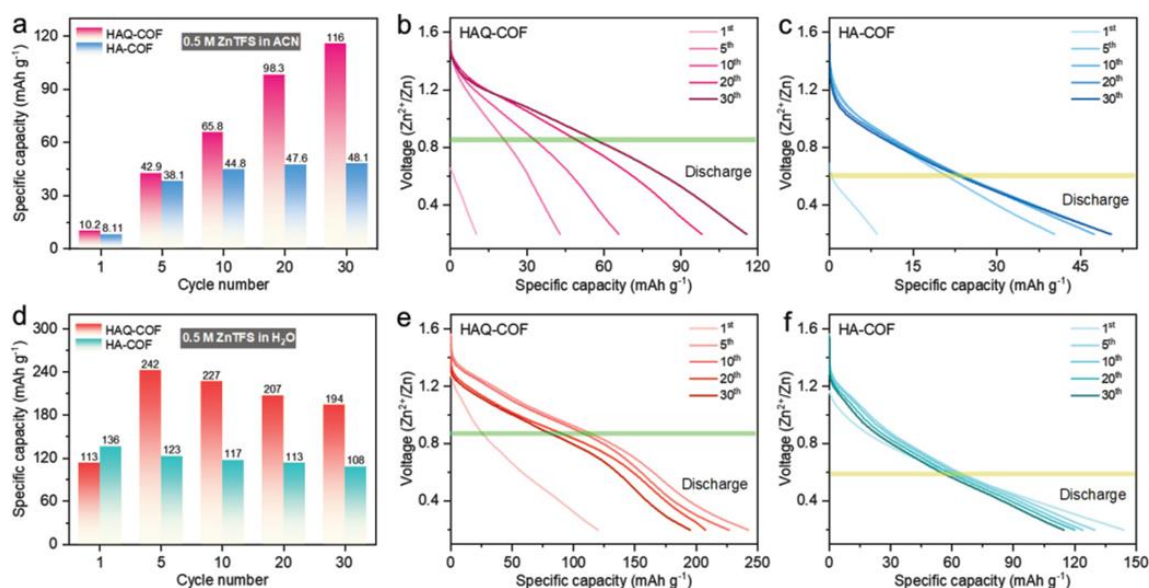
Figure 1.21. Electrochemical performance comparison of HAQ and HA electrodes using GCD measurements at 0.1 A g-1 (a) in non-aqueous and (d) in aqueous solution (b-c) GCD profiles of HAQ-COF and HA-COF electrodes in 0.5 M ZnTFS/ACN, respectively (e,f) GCD profiles of HAQ-COF and HA-COF electrodes in 0.5 M ZnTFS/H$_2$O, respectively.[Source:43]

Besides the COFs materials, CTFs have also demonstrated promising electrochemical performance in AZIBs. In 2022, Tang and co-workers reported the synthesis of CTF-TTPQ polymer through the cyclotrimerization of 2,9-dicyano-5,7,12,14-tetraaza-6,13-pentacenequinone (DCTPQ) in the presence of trifilic acid as catalyst (Figure 1.22).[44]
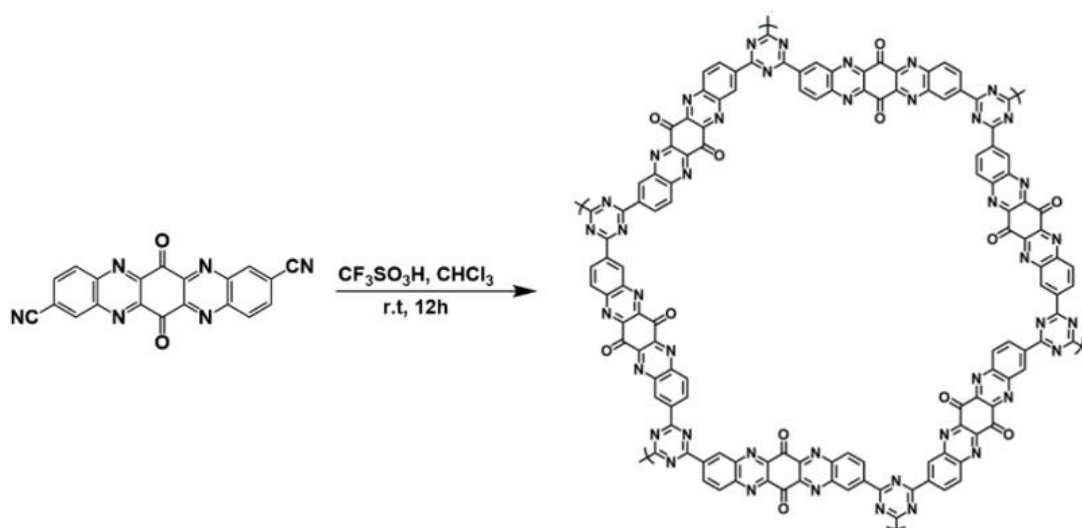
Figure 1.22. Synthesis of CTF-TTPQ from the cyclotrimerization reaction of DCTPQ.[Source:44]

The electrochemical performances of the as-synthesized polymer (CTF-TTPQ) and its monomer (DCTPQ) were evaluated using CV and GCD measurements (Figure 1.23 a-c). The cell incorporating Zn anode, 2.0 M ZnSO$_4$ as electrolyte and CTF-TTPQ as cathode electrode revealed discharged capacity of 404 mA h g^{-1} at a current density of 0.3 A g^{-1} and 204 mA h g^{-1} at 5.0 A g^{-1} (Figure 1.23 c) while DCTPQ cathode only delivered 248 mA h g^{-1} and 58 mA h g^{-1} at the same current densities, respectively. In addition, CTF-TTPQ electrode retrieved %82 of its initial capacity when the current density was shifted from 5.0 A g^{-1} to 0.3 A g^{-1}, indicating its good rate capability of CTF-TTPQ electrode (Figure 1.23 d). The long-term cycling stability of CTF-TTPQ and DCTPQ electrodes were measured at 0.5 A g^{-1}. It was found that % 94 of the capacity was retained over 250 charge/discharge cycles with CTF-TTPQ electrode while the DCTPQ electrode only preserved %50 of its initial capacity at the same current density (Figure 1.23 e). The electrochemical results illustrated the superior redox activity of CTF-TTPQ cathode over its monomer. The unprecedented discharge capacity and cycling stability was attributed to the high abundance of redox center (quinone and pyrazine groups) and insoluble nature of the polymeric network.
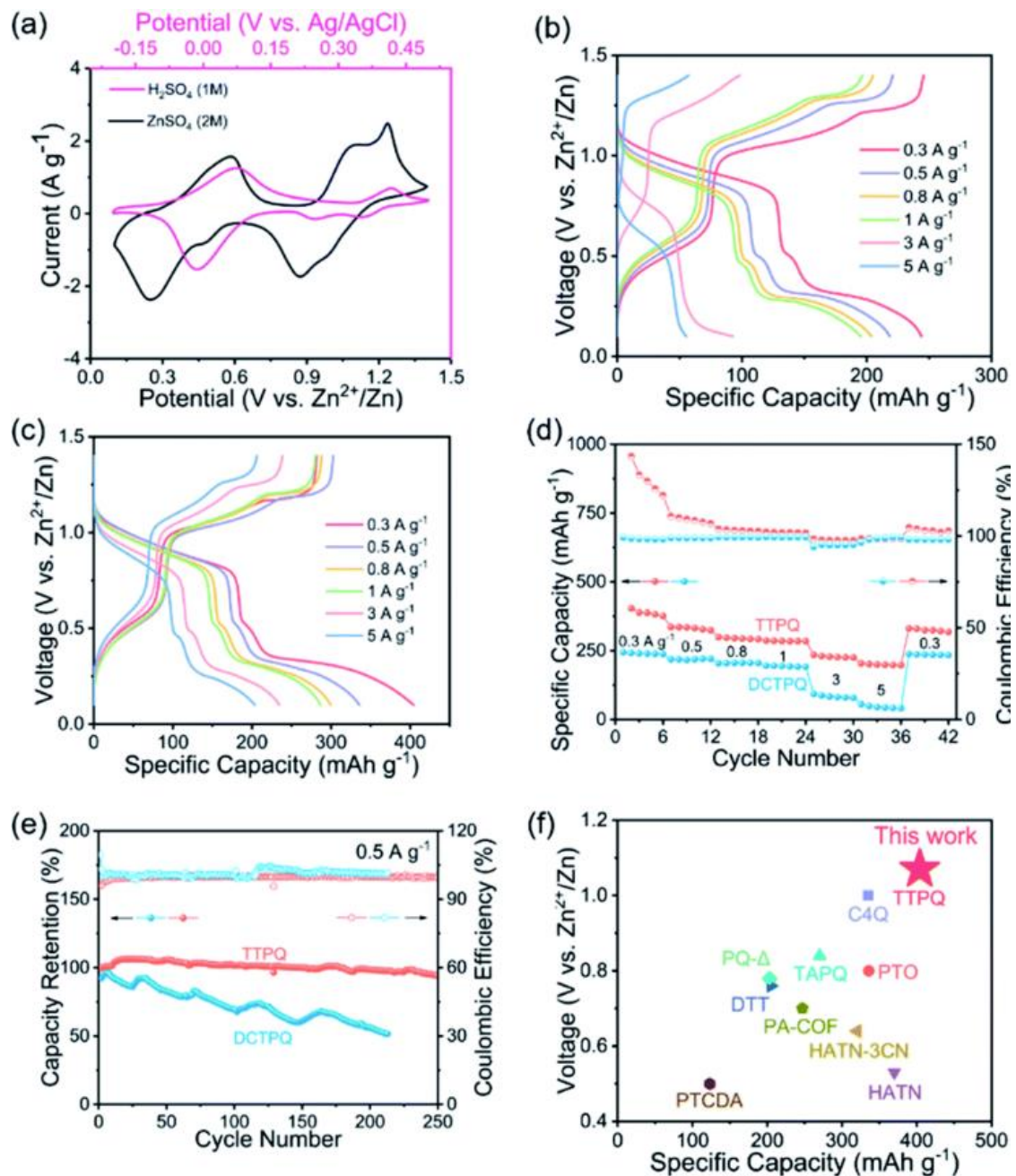
Figure 1.23. Electrochemical performance of CTF-TTPQ (a) CV profile of the electrode in 2.0 M of ZnSO$_4$ and 1.0 M H$_2$SO$_4$ electrolytes (b) GCD measurement of DCTPQ electrode c) GCD measurement of CTF-TTPQ electrode (d) rate capability test and coulumbic efficiency of the CTF-TTPQ and DCTPQ electrodes (e) long-term cycling stability of DCTPQ and CTF-TTPQ electrodes (f) Electrochemical performance comparison of CTF-TTPQ electrode with the reported cathode POP-based cathode materials.[Source:44]

The possible H$^+$/Zn^{2+} co-insertion was investigated to understand the charge storage behavior of CTF-TTPQ electrode. The CV profile of the cell in H$_2$SO$_4$ electrolyte

showed redox peaks at lower potentials compared to the redox potentials of Zn^{2+}. Also, formation of $Zn_4SO_4(OH)_6.5H_2O$, an inorganic salt formed during proton insertion, was detected using SEM and XRD analysis of the discharged electrode, indicating the contribution of protons to the total charge storage. Ex-situ FTIR and XPS spectroscopy determined the functional groups responsible for hosting H^+/Zn^{2+} cations within the CTF-TTPQ structure (Figure 1.24). The FTIR spectra of the discharged electrode showed diminishing C=O and C=N group peaks at 1716 cm^{-1} and 1537 cm^{-1}, respectively, which were restored upon charging, demonstrating the reversibility of Zn^{+2} insertion/desertion. Also, monitoring the compositional changes during charge/discharge states using XPS spectroscopy confirmed that carbonyl and pyrazine groups are the redox-active sites.
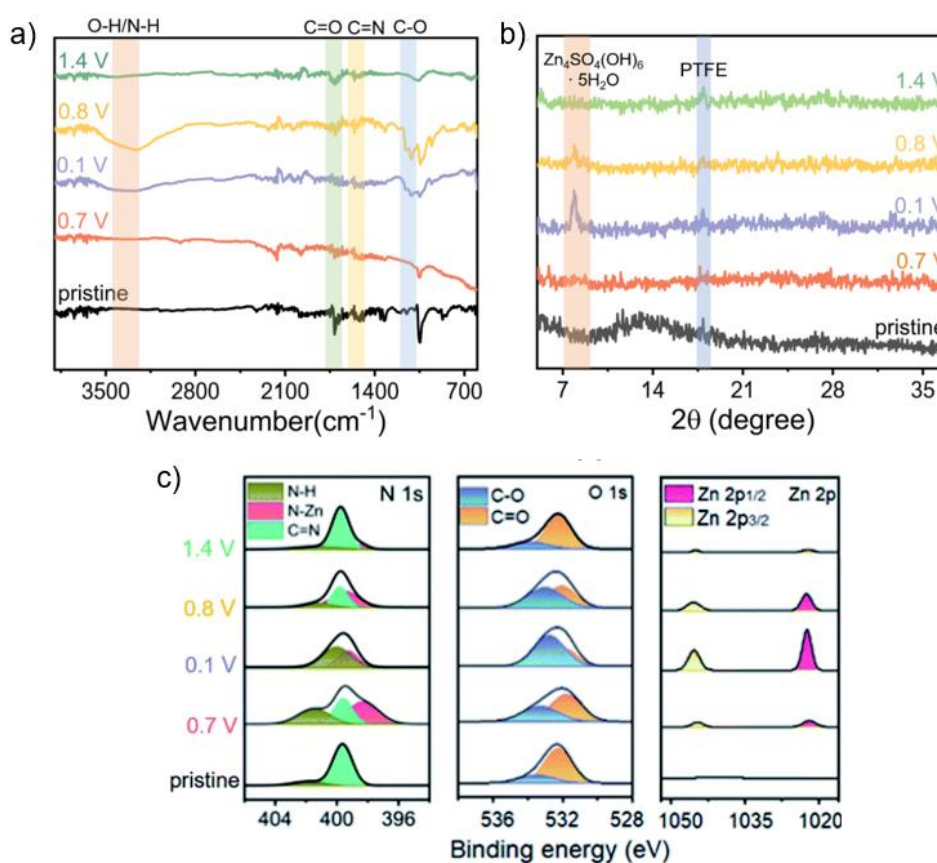
Figure 1.24. Ex-situ measurements of TTPQ electrode during charge/discharge (a) FTIR spectra (b) XRD pattern (c) XPS spectra.[Source:44]

CHAPTER 2

EXPERIMENTAL STUDY

2.1 General Materials

The starting materials and solvents were purchased from Sigma Aldrich, Tokyo Chemical Industry Co.-TCI, and Fluorochem and used without further purification. Merck alumina/silica gel 60-F254 (Merck 5554) was used to perform thin-layer chromatography (TLC). Column chromatography utilizing Merck Kieselgel 60 H silica gel (70 – 230 mesh) was used to purify the reaction products.

2.2 Instrumentations

2.2.1 Nuclear Magnetic Resonance Spectroscopy (NMR)

Liquid phase ^{1}H NMR and ^{13}C NMR spectra were recorded on a Varian Nuclear Magnetic Resonance Spectrometer using deuterated solvents at room temperature (400 MHz for ^{1}H NMR and 100 MHz for ^{13}C NMR). Chemical shifts and coupling constants were reported in ppm and Hz, respectively. Solid-state Cross-Polarization Magic Angle Spinning ^{13}C Nuclear Magnetic Resonance Spectra (CP-MAS ^{13}C NMR) were recorded at room temperature on a Bruker 500 MHz solid-state spectrometer.

2.2.2 Fourier Transform Infrared Spectroscopy (FT-IR)

Perkin-Elmer 65 FT-IR spectrometer was used to collect FT-IR spectra in the transmission mode at room temperature. The spectra were acquired using KBr pellets at a scan rate of 4 cm^{-1} between 4000-400 cm^{-1} intervals.

2.2.3 Powder X-ray Diffraction (PXRD)

PXRD diffractograms were recorded on Philips X'Pert Pro using Cu-Kα (k = 0.154 nm) radiation source at 45 kV and 40 mA. The patterns were collected between 2°– 60° 2Θ with a step size of 0.02.

2.2.4 Scanning Electron Microscope (SEM) and Energy Dispersive X-ray Spectroscopy (EDX)

Field emission SEM images and Energy Dispersive X-ray Spectroscopy (EDX) for elemental mapping of carbon, oxygen, zinc, and sulfur were acquired using ZEISS EVO10 at 1.0-2.0 kV for SEM analysis and 10 – 20 kV for EDX analysis.

2.2.5 Thermogravimetric Analysis (TGA)

Thermogravimetric analysis (TGA) was carried out using a Q 500 analyzer (TA Instruments). The sample was loaded on a platinum pan and heated with a heating rate of 10 $^{\circ}$C min^{-1} for 900 $^{\circ}$C under nitrogen flow.

2.2.6 Gas Adsorption Measurements

N_2 adsorption and desorption isotherms were acquired using a Micromeritics ASAP 2020 surface area and porosity analyzer at 77 K. The samples were activated before collecting the sorption data by degassing the sample for 12 h at 120 °C under a dynamic vacuum. The sample's surface area was calculated using Brunauer-Emmett-Teller (BET) equation. The valid relative pressure range for BET calculation were determined with Rouquerol plots. The total pore volume was determined between a relative pressure range (*P/P$_0$*) of 0.10-0.99.

2.2.7 X-ray Photoelectron Spectroscopy (XPS)

X-ray photoelectron spectra (XPS) were acquired using a ThermoFisher, K-alpha spectrometer. The samples were covered and pressed on copper tape before the analysis. The binding energy calibration was performed by setting the adventitious carbon C 1s peak to 284.6 eV.

2.3 Sample Preparation and Instrumentation for Electrochemical Measurements

2.3.1 Preparation of Cathode Electrode

To prepare the cathode, rPOP was mixed with additives in a certain proportion to increase the conductivity of the electrode. For this purpose, rPOP was blended with super P carbon black (conductive reagent) and polytetrafluoroethylene (PTFE, binder) in ethanol to make a homogeneous slurry mixture with a percent weight ratio of 70, 20 and 10, respectively. A dough was obtained from the slurry and punched to make a disc-like electrode with a diameter of 8.0 mm. The as-prepared electrode was dried in the oven at 80 $^\circ$C for 12 hours, and the mass of dried electrodes was about 1.0-2.0 mg. The discharge capacities were calculated using the mass of rPOP in the electrode.

2.3.2 Assembling the Electrochemical Cell

The electrochemical performance of the rPOP cathode was studied using Swagelok-type cells with two electrode configurations. The cells were assembled with an 8 mm diameter of zinc foil as the anode, 1.0 M $ZnSO_4$ solution as the electrolyte, a Whatman filter paper as a separator, and a cathode electrode comprising the rPOP, respectively. The cells were capped at room temperature.

2.3.3 Sample Preparation for in/ex-situ Analysis and Instrumentation

Cyclic voltammetry (CV) profiles of the cells were collected with a Bio-Logic VMP3e potentiostat/galvanostat instrument between the potential window of 0.1 to 1.6 V. Galvanostatic charge/discharge measurements were performed using LANDT-CT3002A battery-cycler instrument between a potential window of 0.1 to 1.6 V. To study structural changes during charge/discharge measurements, ex-situ FT-IR, XPS, and SEM experiments were performed. The cells were paused at 0.1 and 1.6 V to examine the electrode at discharged and charged states. The electrodes were gently washed with water and dried at 80 °C for 12 hours. A pinch of the cathode was cut and pelletized with KBr for the FT-IR analysis, while the dried electrodes were used as it was for the XPS and SEM/EDX analysis. The in-situ XRD measurements were carried out in a coin cell installed on a Rigaku R-AXIS IV diffractometer. A tiny hole was made in the coin cell casings, Zn anode, and separator to direct the X-ray beam to the rPOP cathode. During the acquisition, the coin cell was cycled three times at a constant current density of 0.1 A g^{-1}, with XRD data acquired every 20 minutes.

2.4 Synthesis Section

2.4.1 Synthesis of 5,12-naphthacenequinone (Model Compound)
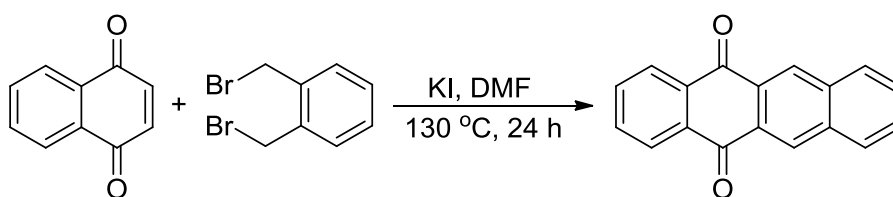
A 50 mL of Schlenk tube was charged with α,α′-dibromo-o-xylene (150 mg, 0.567mmol), 1,4- naphthoquinone (90 mg, 0.567 mmol), and DMF (7.5 mL) at 25 °C under argon atmosphere. The reaction mixture was heated to 90 °C before adding potassium iodide (757 mg, 4.56 mmol), which was then heated to 130 °C and stirred for 24 hours. The resulting mixture was poured onto iced water, and precipitates were collected using a fritted funnel. The crude product was washed with cold methanol and

dried in the oven at 70 °C overnight to obtain 5,12-naphthacenequinone, model compound (yellow solid, 104 mg, 71%). ^{1}H NMR (400 MHz, CDCl$_3$, 25 °C) δ (ppm)= 8.87 (s, 2H), 8.40 (dd, J = 5.8, 3.3 Hz, 2H), 8.11 (dd, J = 6.3, 3.2 Hz, 2H), 7.83 (dd, J = 5.8, 3.3 Hz, 2H), 7.71 (dd, J = 6.3, 3.2 Hz, 2H). ^{13}C NMR (100 MHz, CDCl$_3$, 25 °C): δ (ppm)= 183.0, 135.2, 134.5, 134.2, 130.2, 129.8, 129.6, 129.5, 127.5.

2.4.2 Synthesis of 1,4,5,8-anthracenetetrone (Monomer)
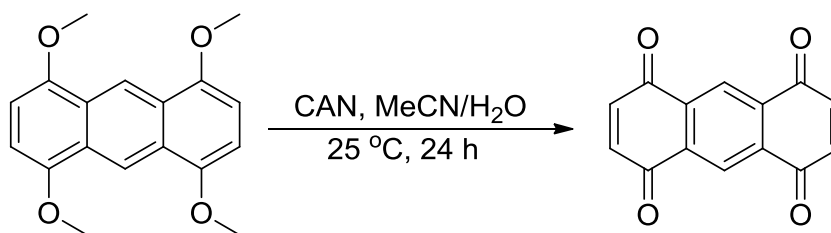
1,4,5,8-tetramethoxy-anthracene was synthesized following the reported procedure in the literature.[62] A 50 mL round bottom flask was charged with cerium ammonium nitrate (5.8 g, 10.6 mmol) and water (10 mL). Subsequently, 1,4,5,8-tetramethoxy-anthracene (0.575 g, 1.93 mmol) in acetonitrile (15 mL) was added dropwise, and the reaction mixture was stirred at 25 °C for 24 hours. After the completion of the reaction, the suspension was centrifuged, extracted with dichloromethane, and dried over MgSO$_4$, and the solvent was evaporated under reduced pressure. The crude product was subjected to column chromatography to yield 1,4,5,8-anthracenetetrone, monomer (red solid, 183 mg, 40%). ^{1}H NMR (400 MHz, CDCl$_3$, 25 °C) δ (ppm) = δ 8.82 (s, 2H), 7.14 (s, 4H). ^{13}C NMR (100 MHz, CDCl$_3$, 25 °C): δ (ppm) = 183.3, 139.4, 135.12, 125.8.

2.4.3 Synthesis of Redox-Active Porous Organic Polymer (rPOP)

rPOP
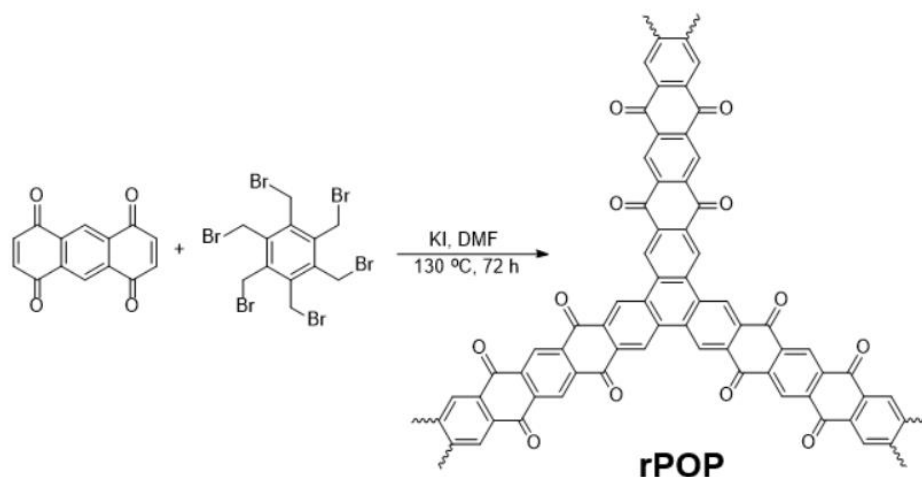
A 50 mL of Schlenk tube was charged with 1,4,5,8-anthracenetetrone monomer (150mg, 0.63 mmol), hexakis(bromomethyl)benzene (267 mg, 0.42 mmol), and DMF (15 mL) at 25 °C under argon atmosphere. The reaction mixture was heated to 90 °C before adding potassium iodide (1.13 g, 6.84 mmol), which was then heated to 130 °C and stirred for 48 hours. The suspension was filtered using a fritted funnel and washed excessively with DMF, water THF, and methanol. The solid was dried at 80 °C in the oven for 12 hours to afford the rPOP (brown solid, 168 mg, 80%).

CHAPTER 3

RESULTS AND DISCUSSION

Synthetic pathways for preparing rPOP and model compound are illustrated in Figure 3.1. The reaction method used in this study does not require a heavy metal-containing catalyst, making these reactions economically viable and environmentally friendly. Additionally, quinone compounds are notorious for having low solubility. Therefore, for a successful polymerization, the high solubility of the oligomers and reaction efficiency are crucial parameters. Firstly, the model compound 5,12-naphthacenequinone was synthesized by subjecting naphthoquinone to a modified version of the Diels-Alder reaction with α,α'-dibromo-o-xylene. The purpose of synthesizing the model compound is to test the feasibility of the reaction and establish ideal conditions for polymerization. The same reaction strategy was used to produce the targeted polymeric structure, rPOP, by reacting hexakis(bromomethyl)benzene with 1,4,5,8-anthracenetetrone conditions, which afforded the rPOP with high yield (Figure 3.1).
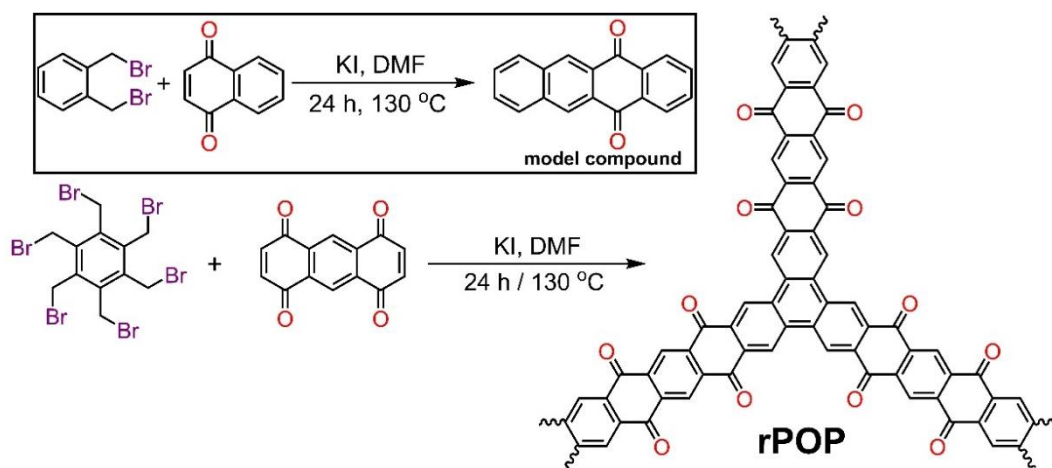
Figure 3.1. Synthetic route for the preparation of model compound and rPOP.

3.1 Characterization and Electrochemical Performance

3.1.1 Characterization of Redox Active Porous Organic Polymer (rPOP)

The successful formation of the desired polymers was confirmed by solid-state cross-polarization magic angle spinning (CP/MAS) ^{13}C NMR spectroscopy, Fourier-transform infrared (FT-IR) spectroscopy, and X-ray photoelectron spectroscopy (XPS). Solid state ^{13}C NMR spectrum of rPOP shows a broad resonance signal located around 120-145 ppm attributed to the aryl groups' carbon atoms. The carbon atom of the carbonyl group is recognized from its distinct resonance signal at 180 ppm. Additionally, the model compound's ^{13}C spectra aligned precisely with the ^{13}C NMR spectra of the rPOP (Figure 3.2).
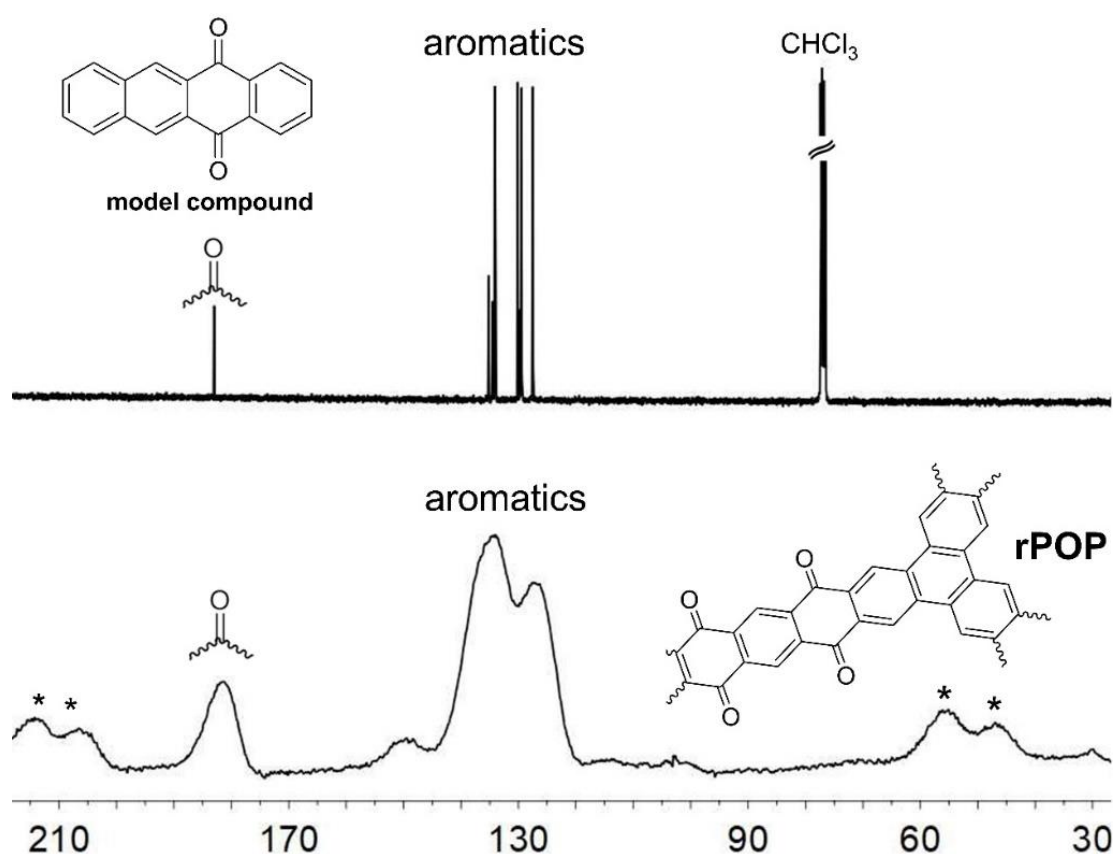
Figure 3.2. Liquid phase ^{13}C NMR spectrum of the model compound and CP/MAS solid-state ^{13}C NMR spectrum of rPOP.

In the FT-IR spectra, weakening of the C-Br stretching vibrations of hexakis(bromomethyl)benzene around 600 cm^{-1} indicates that the reactants are consumed during the Diels-Alder reaction. Also, the emergence of characteristic carbonyl stretching at 1700 cm^{-1} in the rPOP is consistent with the proposed structure (Figure 3.3).
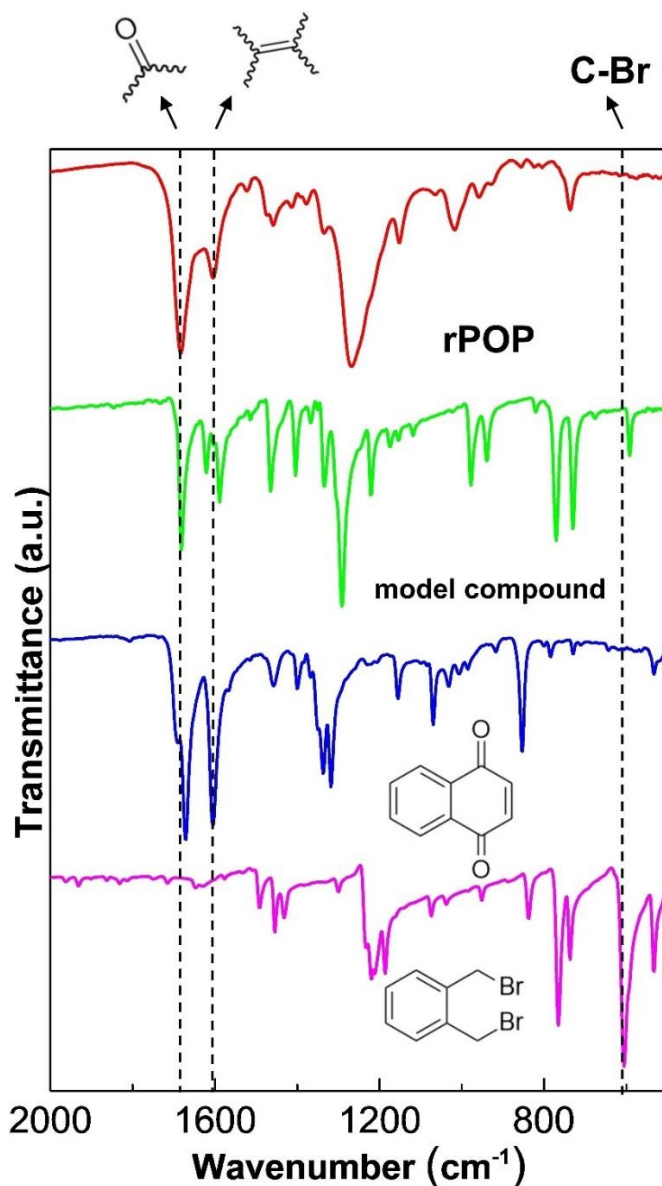
Figure 3.3. FT-IR spectra of rPOP, model compound, naphthoquinone and α,α′ dibromo o-xylene.

The chemical composition and bonding types are investigated using the XPS technique. The survey scan analysis is used as a starting point to determine which elements are present in the polymeric structure. The reaction by-products, which include

potassium, iodine, and nitrogen elements, should not appear in the survey analysis. The appearance of only the 1s signals of oxygen and carbon atoms are detected in the model compound and rPOP, which shows the efficient purification of the model compound and rPOP. The absence of bromine signals also shows that the polymerization reaction was successfully completed (Figure 3.4a and Figure 3.4d). High-resolution XPS spectra were investigated to determine the chemical state of the carbon and oxygen atoms. Deconvolution of the high-resolution C 1s spectrum of rPOP into two peaks at 284.6 and 287.3 eV can be attributed to carbon atoms in aromatic rings (C=C) and carbon atoms connected to oxygen atoms in the carbonyl group (C=O), respectively (Figure 3.4b). Deconvolution of the high-resolution O1s spectrum of rPOP into two peaks at 531.6 and 533.4 eV can be attributed to oxygen atoms in the carbonyl group (C=O) and oxygen atoms of water that is trapped in the pores of the rPOP), respectively (Fig. 3.4c). A similar trend is observed for the high-resolution carbon and oxygen atoms spectra in the model compound. Deconvolution of the high-resolution C 1s spectrum of the model compound into two peaks at 284.6 and 287.2 eV can be attributed to carbon atoms in aromatic rings (C=C) and carbon atoms connected to oxygen atoms in the carbonyl group (C=O), respectively (Figure 3.4e). Deconvolution of the high-resolution O1s spectrum of rPOP into two peaks at 531.5 and 533.3 eV can be attributed to oxygen atoms in the carbonyl group (C=O) and oxygen atoms of water that is trapped in the pores of the rPOP), respectively (Figure 3.4f).
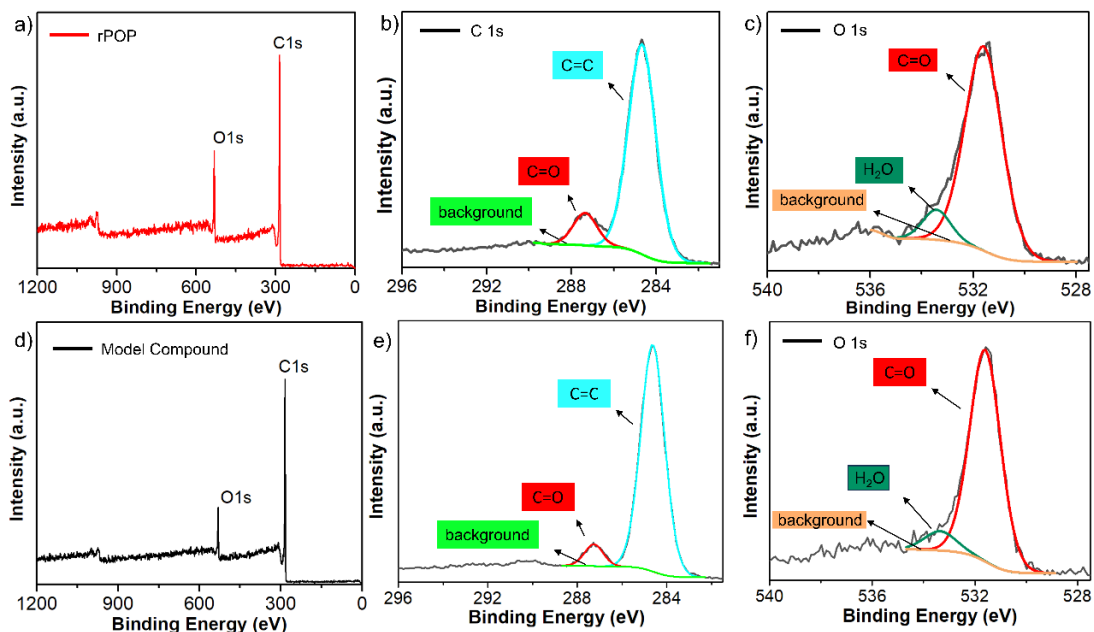
Figure 3.4. XPS analysis of rPOP a) survey spectrum of rPOP b,c) C 1s and O 1s high resolution spectra of rPOP d) survey spectrum of model compound e,f) C 1s and O 1s high-resolution spectra of the model compound.

N$_2$ sorption measurements at 77 K were performed to investigate the porosity of the polymer (Figure 3.5 a). The rPOP exhibits type I isotherms with a steep uptake behavior at low partial pressure. This steep uptake indicates that the material is microporous. The permanent surface area is calculated using Brunauer–Emmett–Teller (BET) equation. The valid relative pressure region was determined using the Rouquerol plot (Figure 3.5 c) The BET calculations showed that the material possesses a specific surface area of 737 m^2 g^{-1} (Figure 3.5 d). Pore size distribution analysis is carried out using Non-local Density Functional Theory (NLDFT). The results show a homogeneous pore size distribution with a peak at 1.0 nm (Figure 3.5b).
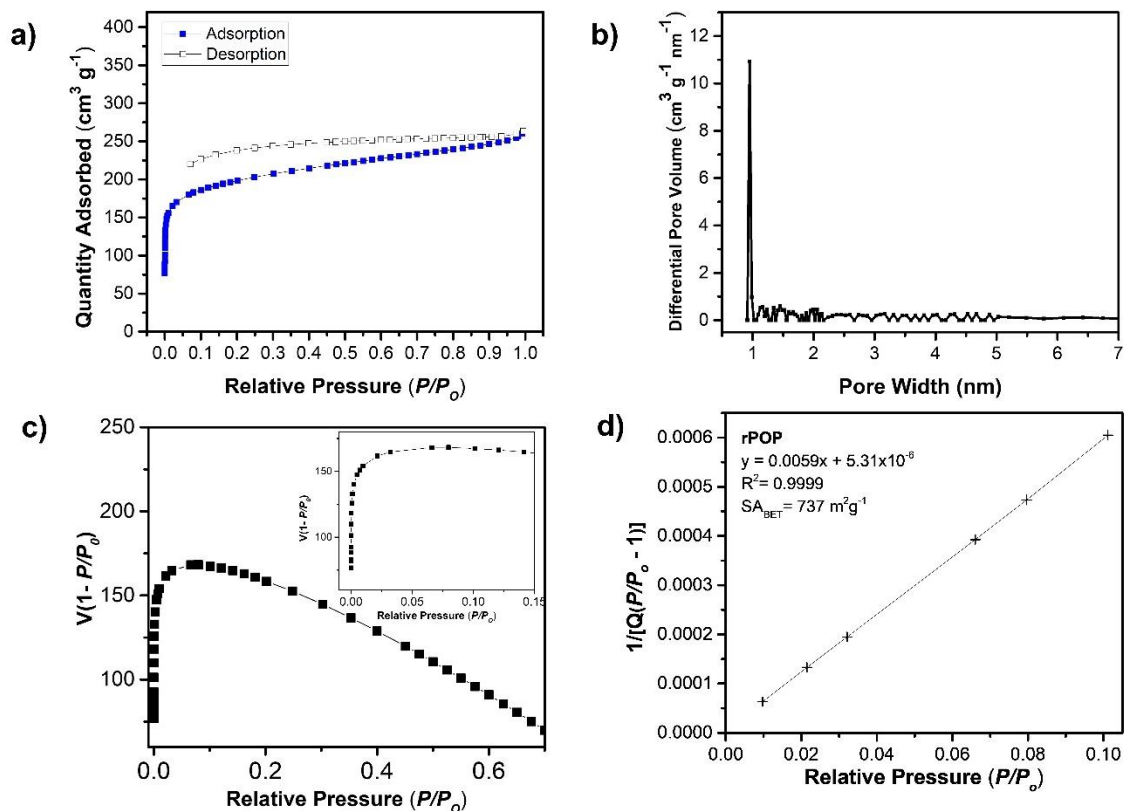
Figure 3.5. a) Adsorption/Desorption isotherm of rPOP collected using N_2 at 77 K b) Pore size distribution c) Rouquerol plot d) BET plot of rPOP according to the valid pressure range.

The thermal stability of the rPOP was studied by thermogravimetric analysis (Figure 3.6). The sample was degassed before the analysis to remove the trapped organic solvents and moisture. It is clear from the graph that the polymer maintains structural integrity and does not exhibit any mass loss up to 400 °C. Then, up to 500 °C, there are only minor mass losses, about %10 , but after that point, there is a significant mass loss, and only %30 mass percentage is retained at 700 °C. These findings show the superior thermal stability of rPOP up to 400 °C.
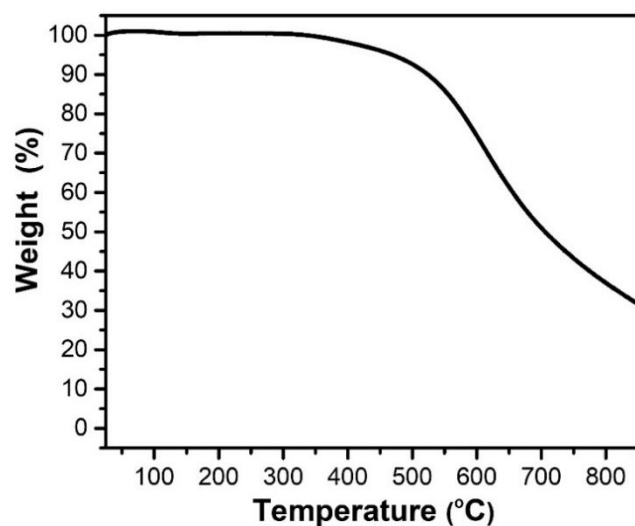
Figure 3.6. TGA analysis under N_2 atmosphere.

The particle morphology of rPOP was evaluated by scanning electron microscopy (SEM) (Figure 3.7). SEM images show the presence of spherical particles that has particle diameters between 200 nm to 300 nm. Additionally, elemental mapping using Energy Dispersive X-Ray Spectroscopy (EDX) was carried out in the same SEM image region. EDX analysis results reveal that carbon and oxygen atoms are distributed uniformly throughout the polymer.
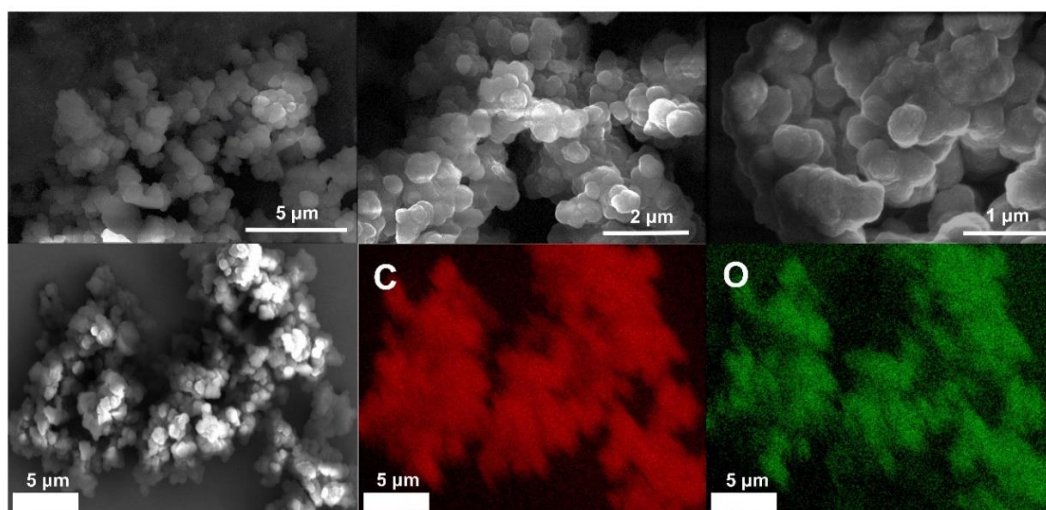
Figure 3.7. SEM-EDX images of rPOP.

Powder X-ray diffraction analysis (PXRD) is performed to determine whether the polymeric network exhibits crystallinity (Figure 3.8). The absence of sharp peaks in the diffractogram indicates that the rPOP is amorphous. According to Bragg's law, the broad peak at 26° corresponds to about 0.36 nm distance and represents the stacking behavior of the rPOP sheets.
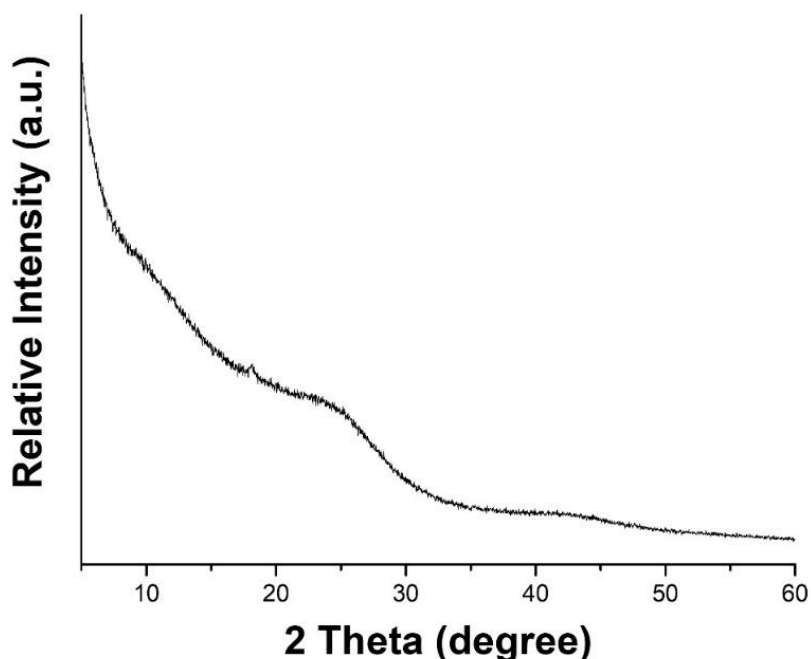
Figure 3.8. PXRD pattern of rPOP.

3.1.2 Electrochemical Performance of rPOP

First, the reversibility of ions insertion and extraction on the rPOP is evaluated with cyclic voltammetry (CV) (Figure 3.9). The CV measurements are recorded at various scan rates between the potential window of $0.1 - 1.6$ V. The voltammograms show one broad oxidation peak at 0.95 V and three reduction peaks at 0.35, 0.68, and 0.83 V, corresponding to the redox reaction at the cathode and confirming the rPOP electrode's reversibility. It is worth noting that when the scan rate increases, the anodic/cathodic peak currents increase with minimal variations in the peak positions, indicating the fast kinetics and reversibility of ions insertion and extraction.
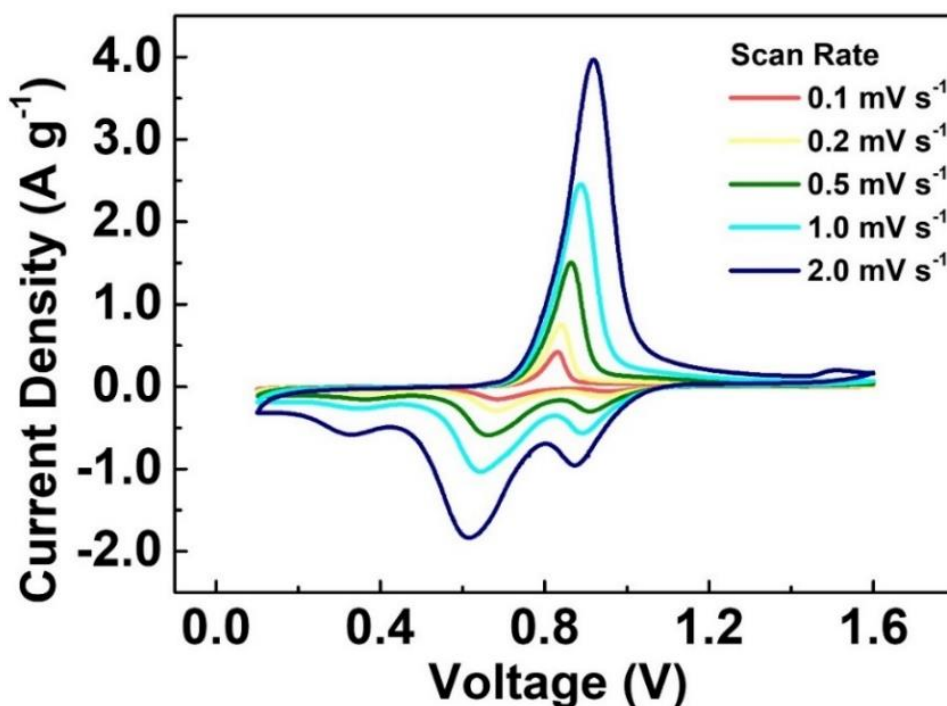
Figure 3.9. CV curves collected at various scan rates.

To investigate the charge storage capacity, rate capability, and cycling stability of the rPOP electrode, galvanostatic charge, and discharge (GCD) measurements are carried out (Figure 3.10). Firstly, the capacity of the rPOP electrode is assessed at different current densities. The cell containing rPOP cathode delivered discharged capacities of 120 mAh g^{-1} at a current density of 0.1 A g^{-1}. This value demonstrates the excellent charge storage capacity of the rPOP in AZIBs. It is worth mentioning that the slope of charge and discharge plateaus are close to zero, indicating that the rPOP electrode's working mechanism resembles the battery-type system that relies on the diffusive charge storage behavior. This charge storage behavior is rare in AZIBs and provides a continuous voltage output which is advantageous in applications.
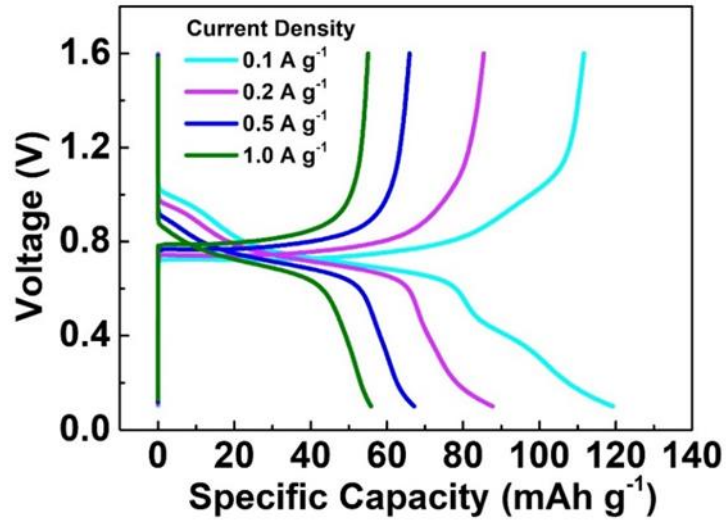
Figure 3.10. Galvanostatic charge/discharge measurements at different current densities.

The rate capability test is conducted on the rPOP electrode at different current densities (Figure 3.11). The rPOP electrode delivered discharged capacities of 89, 69, 58 mAh g^{-1} when the current density was increased to 0.2, 0.5 and 1.0 A g^{-1}, respectively. It is important to note that when the current density is switched back to 0.1 A g^{-1} from 1.0 A g^{-1}, %95 of the original capacity value at 0.1 A g^{-1} (120 mAh g^{-1}) was recovered. This finding illustrates the high-rate performance of the rPOP electrode in AZIBs.
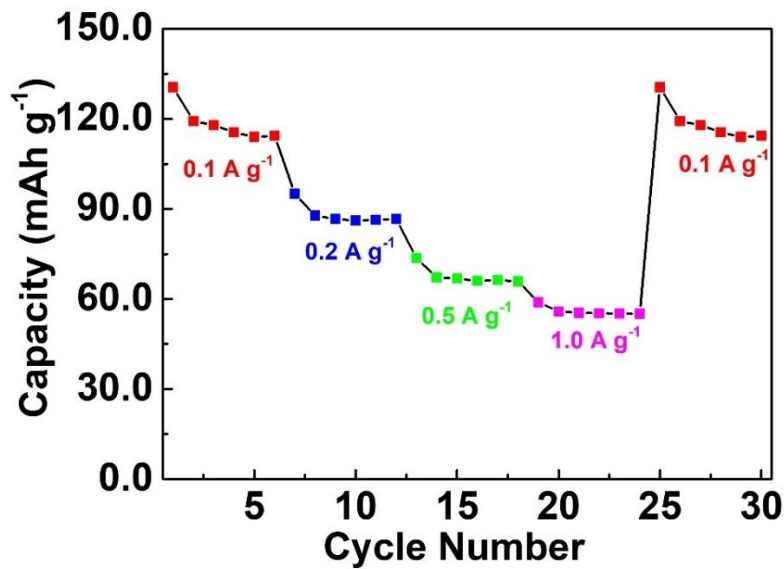
Figure 3.11. Rate performance of rPOP cathode.

The ultralong cycle life of the rPOP electrode is realized at different current densities (Figure 3.12). The cell incorporation rPOP electrode retained %95 of its original capacity over 1000 charge/discharge cycles with a Coulombic efficiency of %100. When the cell was cycled 30000 times at the current density of 2.0 A g^{-1}, %66 of its initial capacity was retained with a reasonable Coulombic efficiency. These results reveal that the rPOP electrode in AZIBs has improved long-term cycling stability, and the structural integrity of the rPOP electrode is preserved during extremely extended charge/discharge cycles.
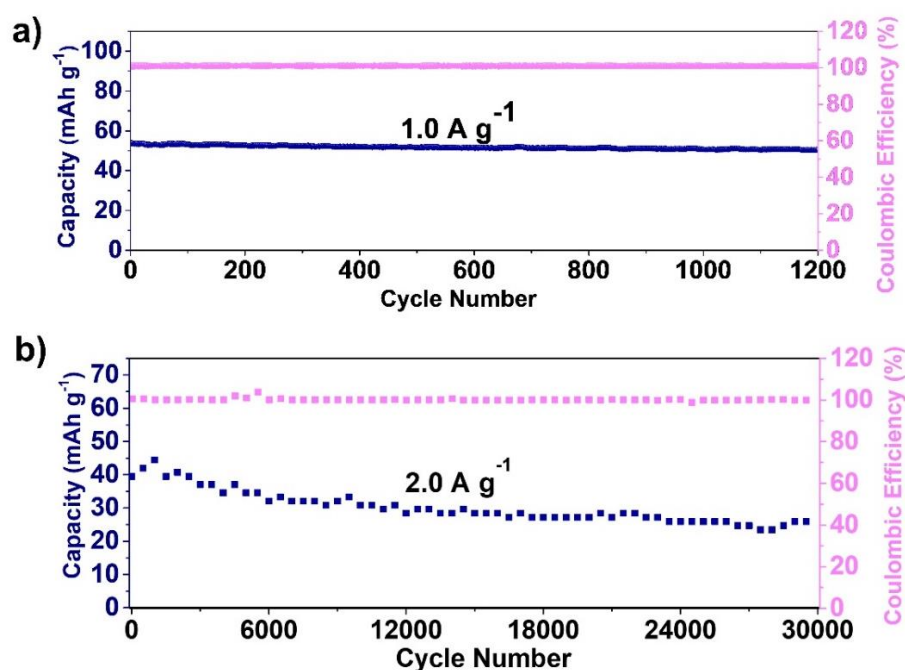
Figure 3.12. Cycle life of rPOP cathode a) at a current density of 1.0 A g^{-1} b) at a current density of 2.0 A g^{-1}.

3.1.2.1 Electrochemical Kinetics of rPOP

Conducting CV measurements at various scan rates discloses the electrochemical kinetics of rPOP cathode (Figure 3.13. a). The power-law equation, $i = av^b$, provides a means to estimate the b-value by examining the relationship between the peak current (i) in Amper (A) and the scan rate (v) in volts per second (V s^{-1}). The b-value ranges from 0.5 to 1.0. A b-value closer to 0.5 indicates a battery's characteristic charge storage behavior, where charge storage is controlled by a diffusive-controlled process, also

known as a faradic process. Conversely, a *b*-value closer to 1.0 suggests that charge storage is governed by a capacitive-controlled process, which is non-faradaic. In this context, it becomes possible to estimate the charge storage behavior of electrode reactions by analyzing the *b*-values, which are obtained from the linear slope of log *i* versus log *v*. The *b*-values are determined as follows: for the oxidation peak at 0.95 V, the *b*-value is calculated as 0.75, and for the reduction peaks at 0.35, 0.68, and 0.83 V, the corresponding *b*-values are 0.93, 0.82, and 0.82, respectively (Figure 3.13. b-d).
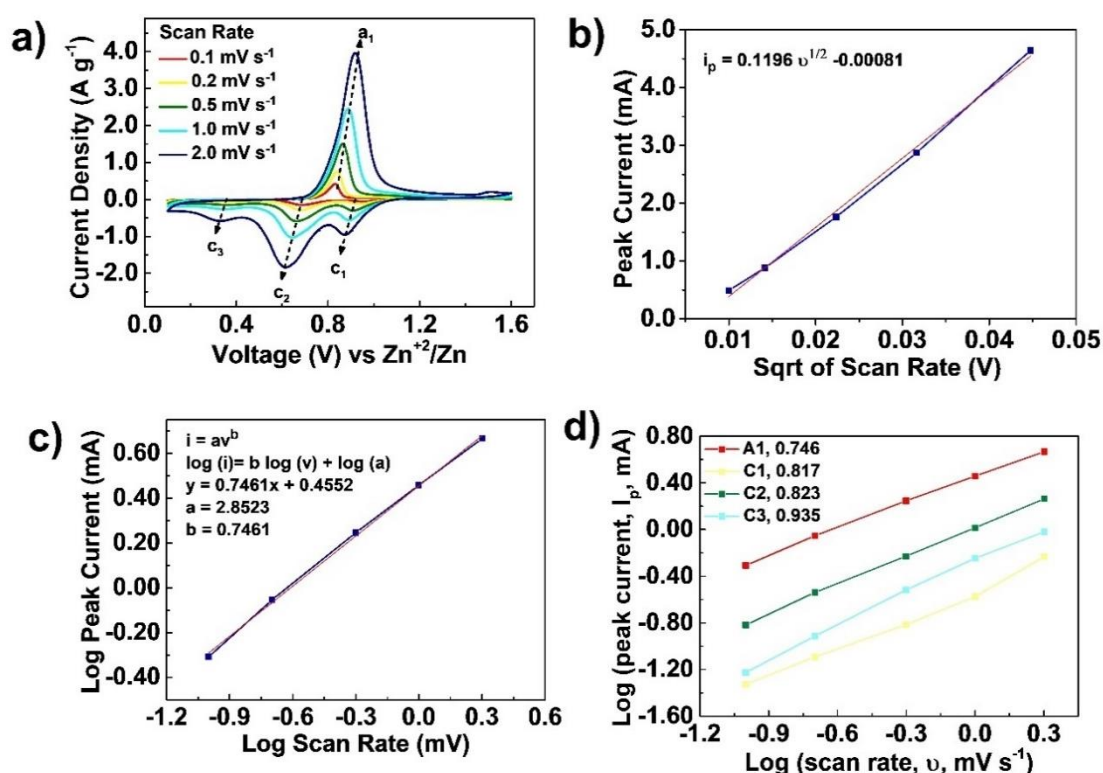
Figure 3.13. Electrochemical kinetics of rPOP a) CV curves collected at various scan rates b) Relationship between peak current and scan rate c) b-value for the anodic peak d) b-values for anodic and cathodic peaks concerning power law equation.

The observed *b*-values indicate that rPOP is affected by both diffusive and capacitive charge storage mechanisms. While *b*-values greater than 0.8 typically indicate a predominant contribution of the capacitive process over the diffusive-controlled charge storage mechanism, rPOP exhibits lower *b*-values compared to other quinone-containing POPs. This suggests a more substantial involvement of faradaic redox reactions in the charge storage of rPOP. Furthermore, to quantitatively distinguish between the diffusion-

controlled and capacitive contributions at specific potentials, the equation [$i(V) = k_1v + k_2v^{1/2}$], introduced by Dunn and colleagues,[63] is utilized. In this equation, the total current (i) at a given potential (V) can be described as a combination of two distinct mechanisms: capacitive effects (k_1v) and diffusion-controlled insertion ($k_2v^{1/2}$), where v is scan rate and i is the peak current.
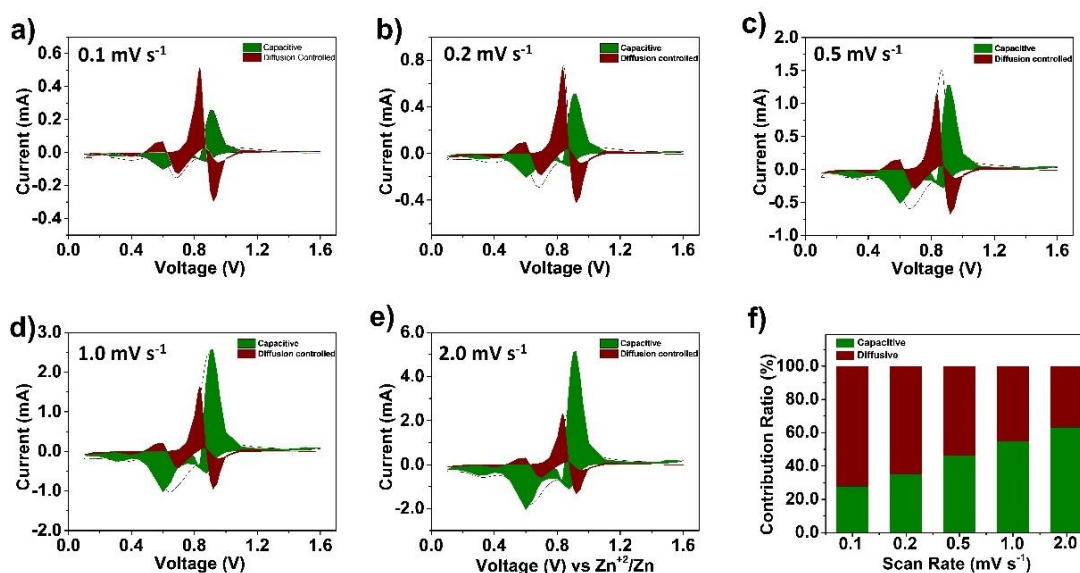
Figure 3.14. The quantitative relationship between diffusion-controlled and capacitive contributions of rPOP cathode.

As depicted in Figure 3.14, the corresponding diffusive contribution values for scan rates of 0.1, 0.2, 0.5, 1.0, and 2.0 mV s^{-1} are 72%, 65%, 54%, 45%, and 37%, respectively. These findings indicate a gradual decrease in the diffusive contribution with higher scan rates. In contrast to recently reported POP-based cathodes, it is interesting that rPOP exhibits a substantially more significant contribution from the diffusive-controlled charge storage.

3.1.2.2 Charge Storage Mechanism of rPOP

Both ex-situ and in-situ methods are employed to examine the charge storage mechanism and structural changes that occur during the charge storage of the rPOP cathode. At the initial stage, identifying the functional groups responsible for binding of

ions is accomplished by analyzing the discharged electrode using FT-IR analysis (Figure 3.15).
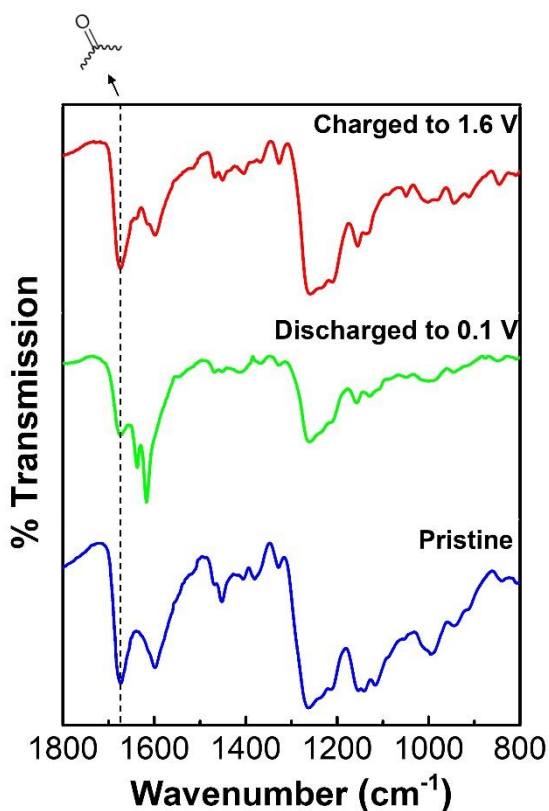
Figure 3.15. FT-IR spectra of rPOP electrode at different states.

A significant decrease in the intensity of the carbonyl stretching band around 1700 cm^{-1} is observed in the electrode discharged at 0.1 V, suggesting that the quinone moieties serve as the redox-active sites. This decrease is reversed, and the peak is recovered when the electrode is charged to 1.6 V. The recovery of the carbonyl stretching band during the recharge process demonstrates the reversibility of ions accommodation once again.

The structural change in the morphology of the rPOP electrode during charge/discharge cycles is investigated using SEM (Figure 3.16). SEM image of the discharge electrode reveals the presence of platelet-shaped structures and suggests the formation of a zinc hydroxy sulfate salt, specifically $[Zn_4SO_4(OH)_6 \cdot 5H_2O]$. This salt is believed to be a side-product formed due to the insertion of protons into the cathode during discharge. When the pH of a slightly acidic 1.0 M $ZnSO_4$ electrolyte, with a pH of approximately 4.5, rises above 5.5, the $[Zn_4SO_4(OH)_6 \cdot 5H_2O]$ salt is formed. This salt is

formed because protons are inserted into the cathode, which causes the release of OH⁻ ions into the electrolyte solution and triggers a localized pH increase. To probe the Zn^{2+}/H^+ co-(de)insertion behavior, EDX mapping on the same SEM region were performed. The homogeneous distribution of zinc, sulfur, and carbon and oxygen were observed. The signals of zinc and sulfur almost completely disappear upon charging, thus suggesting both the dissolution of zinc hydroxy sulfate salt and reversible co-(de)insertion of Zn^{2+}/H^+ insertion.
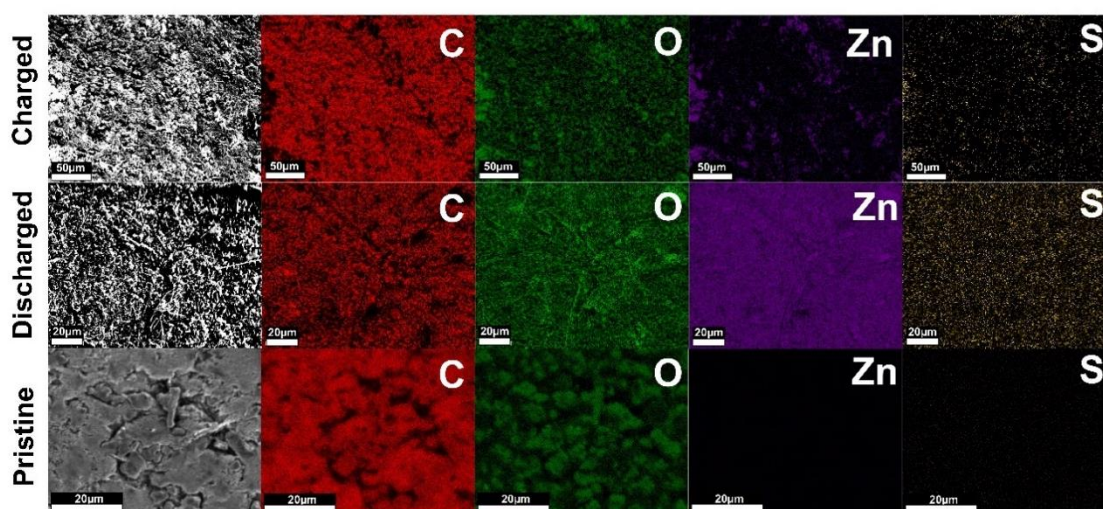
Figure 3.16. SEM/EDX analysis of rPOP electrode at different states.

Also, XPS spectroscopy was performed on the discharged/charged states. The Zn 2p and S 2p signals were observed in the Zn 2p and S 2p high-resolution spectra of discharged electrode at 0.1 V. These signals are drastically attenuated in the charged electrode at 1.6 V. It is worth to note that a tiny fraction of the Zn 2p and S 2p signals remain in the charged electrode, which suggests that the dissolution of the $[Zn_4SO_4(OH)_6 \cdot 5H_2O]$ salt is not fully completed (Figure 3.17).
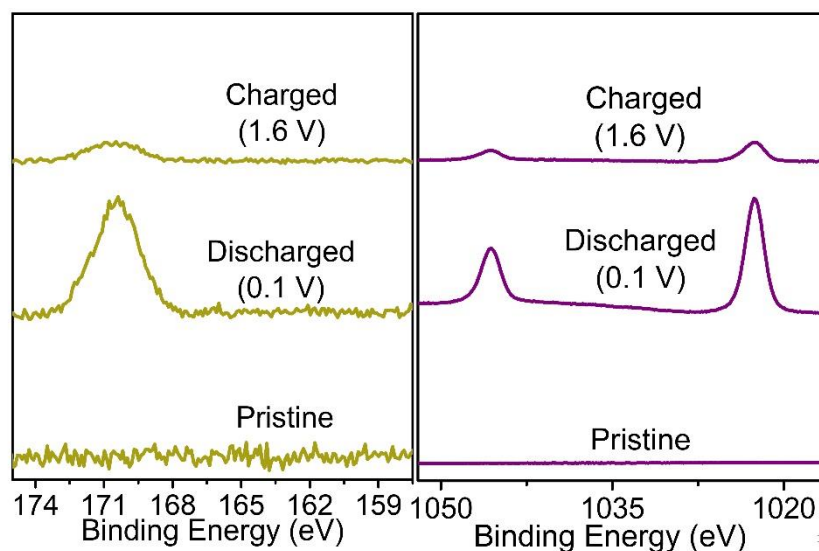
Figure 3.17. XPS analysis of rPOP electrode at different states.

In-situ XRD analysis is carried out to gain insight into the origin of charge storage and follow the Zn^{2+}/H^+ co-insertion behavior. Figure 3.18 shows PXRD profile of the rPOP cathode as a function of voltage. The peaks associated with $[Zn_4SO_4(OH)_6 \cdot 5H_2O]$ undergo stepwise decrease during charging up to 1.6 V, and gradual increase during discharging up to 0.1 V. This finding aligns well with the outcomes obtained from SEM/EDX and XPS analyses of the charged electrode. Furthermore, upon charging and discharging the electrode once again, the reappearance of the characteristic peak of $[Zn_4SO_4(OH)_6 \cdot 5H_2O]$ confirms the reversibility of the precipitation and dissolution of $[Zn_4SO_4(OH)_6 \cdot 5H_2O]$.
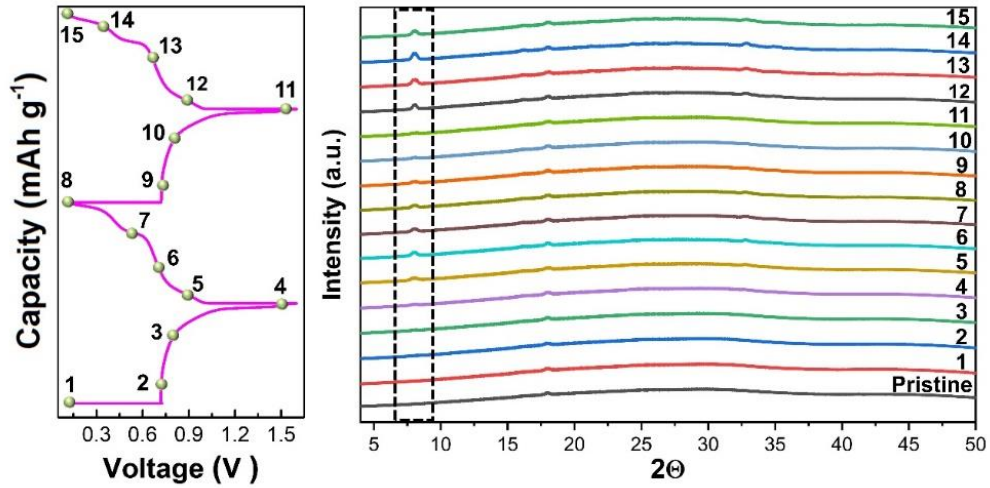
Figure 3.18. In-situ XRD analysis of rPOP electrode at different states.

To quantitatively evaluate the contribution of H^+ insertion to the overall capacity, the rPOP electrode is subjected to CV measurements using a 5×10^{-5} M $H_2SO_{4(aq)}$ electrolyte solution, which provides the same concentration of H^+ as in the 1.0 M $ZnSO_4$ solution (Figure 3.19). The voltammogram reveals a broad oxidation peak at 0.95 V and three reduction peaks at 0.35, 0.68, and 0.83 V, as in the case of 1.0 M $ZnSO_4$ electrolyte solution. By comparing the area under the CV curves, it becomes apparent that Zn^{2+} plays a dominant role in the charge storage process, while H^+ contributes partially to the electrochemical performance. The cell prepared with the 5×10^{-5} M $H_2SO_{4(aq)}$ electrolyte exhibited a capacity contribution of approximately 17% at a scan rate of 2.0 mV s^{-1}.
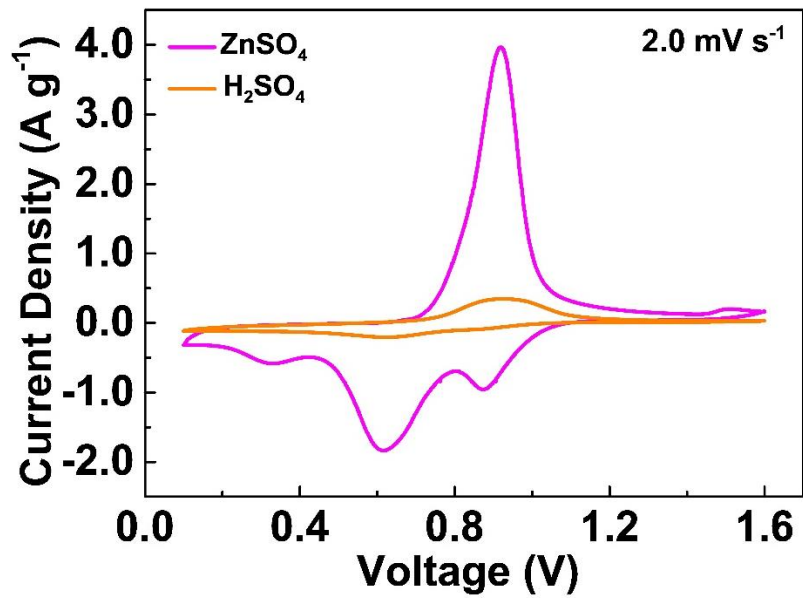
Figure 3.19. CV curves of rPOP electrode collected in $ZnSO_4$ and H_2SO_4 electrolytes.

CHAPTER 4

CONCLUSION

In conclusion, the synthesis of redox-active porous organic polymer (rPOP) using a modified version of Diels-Alder reaction between hexakis(bromomethyl)benzene and 1,4,5,8-anthracenetetrone is reported. The as-prepared polymer is utilized as a cathode material for aqueous zinc-ion batteries (AZIBs). The successful synthesis of the rPOP was validated using FT-IR, solid-state ^{13}C NMR, and XPS spectroscopies. The highly porous nature of the rPOP facilitated the effective diffusion of Zn^{2+}/H^+ ions into the redox-active centers. The structural durability of the rPOP endowed superior cycling stability to the electrochemical cell without significant change in the charge storage capacity and rate performance. The cell incorporating rPOP cathode delivered discharge capacity of 120 mAh g^{-1} at a current density of 0.1 A g^{-1} and the cell retained %66 of its original capacity for 30000 charge/discharge cycles at a current density of 2.0 A g^{-1}. The confirmation of the Zn^{2+}/H^+ (de)insertion, structural changes during charge/discharge cycles, and charge storage mechanism of the rPOP were clearly demonstrated using (ex)in-situ characterizations. These findings unfold the potential of porous organic polymers (POPs) as a cathode material in AZIBs, and we believe this study will stimulate researchers to design and study new POPs as a cathode material for AZIBs.

REFERENCES

1. Dunn, B.; Kamath, H.; Tarascon, J.-M., Electrical Energy Storage for the Grid: A Battery of Choices. Science 2011, 334 (6058), 928-935.

2. Yang, Z.; Zhang, J.; Kintner-Meyer, M. C. W.; Lu, X.; Choi, D.; Lemmon, J. P.; Liu, J., Electrochemical Energy Storage for Green Grid. Chem. Rev. 2011, 111 (5), 3577-3613.

3. Pelegov, D. V.; Pontes, J. Main Drivers of Battery Industry Changes: Electric Vehicles—A Market Overview Batteries [Online], 2018.

4. Zhu, Z.; Jiang, T.; Ali, M.; Meng, Y.; Jin, Y.; Cui, Y.; Chen, W., Rechargeable Batteries for Grid Scale Energy Storage. Chem. Rev. 2022, 122 (22), 16610-16751.

5. Li, M.; Lu, J.; Chen, Z.; Amine, K., 30 Years of Lithium-Ion Batteries. Adv. Mater. 2018, 30 (33), 1800561.

6. Goodenough, J. B.; Park, K.-S., The Li-Ion Rechargeable Battery: A Perspective. J. Am. Chem. Soc. 2013, 135 (4), 1167-1176.

7. Narins, T. P., The battery business: Lithium availability and the growth of the global electric car industry. The Extractive Industries and Society 2017, 4 (2), 321-328.

8. Ponnada, S.; Kiai, M. S.; Krishnapriya, R.; Singhal, R.; Sharma, R. K., Lithium-Free Batteries: Needs and Challenges. Energy & Fuels 2022, 36 (12), 6013-6026.

9. Liu, K.; Liu, Y.; Lin, D.; Pei, A.; Cui, Y., Materials for lithium-ion battery safety. Sci. Adv. 2018, 4 (6), eaas9820.

10. Chen, L.; An, Q.; Mai, L., Recent Advances and Prospects of Cathode Materials for Rechargeable Aqueous Zinc-Ion Batteries. Adv. Mater. Interfaces 2019, 6 (17), 1900387.

11. Song, M.; Tan, H.; Chao, D.; Fan, H. J., Recent Advances in Zn-Ion Batteries. Adv. Funct. Mater. 2018, 28 (41), 1802564.

12. Zampardi, G.; La Mantia, F., Open challenges and good experimental practices in the research field of aqueous Zn-ion batteries. Nat. Commun. 2022, 13 (1), 687.

13. Yuksel, R.; Buyukcakir, O.; Seong, W. K.; Ruoff, R. S., Metal-Organic Framework Integrated Anodes for Aqueous Zinc-Ion Batteries. Adv. Energy Mater. 2020, 10 (16), 1904215.

14. Li, H.; Ma, L.; Han, C.; Wang, Z.; Liu, Z.; Tang, Z.; Zhi, C., Advanced rechargeable zinc-based batteries: Recent progress and future perspectives. Nano Energy 2019, 62, 550-587.

15. Zhang, N.; Chen, X.; Yu, M.; Niu, Z.; Cheng, F.; Chen, J., Materials chemistry for rechargeable zinc-ion batteries. Chem. Soc. Rev. 2020, 49 (13), 4203-4219.

16. Zhang, M.; Liang, R.; Or, T.; Deng, Y.-P.; Yu, A.; Chen, Z., Recent Progress on High-Performance Cathode Materials for Zinc-Ion Batteries. Small Structures 2021, 2 (2), 2000064.

17. Zhong, C.; Liu, B.; Ding, J.; Liu, X.; Zhong, Y.; Li, Y.; Sun, C.; Han, X.; Deng, Y.; Zhao, N.; Hu, W., Decoupling electrolytes towards stable and high-energy rechargeable aqueous zinc–manganese dioxide batteries. Nat. Energy 2020, 5 (6), 440-449.

18. Hu, P.; Zhu, T.; Ma, J.; Cai, C.; Hu, G.; Wang, X.; Liu, Z.; Zhou, L.; Mai, L., Porous V_2O_5 microspheres: a high-capacity cathode material for aqueous zinc–ion batteries. Chem. Commun. 2019, 55 (58), 8486-8489.

19. Wan, F.; Niu, Z., Design Strategies for Vanadium-based Aqueous Zinc-Ion Batteries. Angew. Chem. Int. Ed. 2019, 58 (46), 16358-16367.

20. Zhang, L.; Chen, L.; Zhou, X.; Liu, Z., Towards High-Voltage Aqueous Metal-Ion Batteries Beyond 1.5 V: The Zinc/Zinc Hexacyanoferrate System. Adv. Energy Mater. 2015, 5 (2), 1400930.

21. Yuan, X.; Sun, T.; Zheng, S.; Bao, J.; Liang, J.; Tao, Z., An inverse-spinel Mg_2MnO_4 cathode for high-performance and flexible aqueous zinc-ion batteries. J. Mater. Chem. A 2020, 8 (43), 22686-22693.

22. Guo, Z.; Ma, Y.; Dong, X.; Huang, J.; Wang, Y.; Xia, Y., An Environmentally Friendly and Flexible Aqueous Zinc Battery Using an Organic Cathode. Angew. Chem. Int. Ed. 2018, 57 (36), 11737-11741.

23. Lin, Z.; Shi, H.-Y.; Lin, L.; Yang, X.; Wu, W.; Sun, X., A high capacity small molecule quinone cathode for rechargeable aqueous zinc-organic batteries. Nat. Commun. 2021, 12 (1), 4424.

24. Nam, K. W.; Kim, H.; Beldjoudi, Y.; Kwon, T.-w.; Kim, D. J.; Stoddart, J. F., Redox-Active Phenanthrenequinone Triangles in Aqueous Rechargeable Zinc Batteries. J. Am. Chem. Soc. 2020, 142 (5), 2541-2548.

25. Peng, H.; Xiao, J.; Wu, Z.; Zhang, L.; Geng, Y.; Xin, W.; Li, J.; Yan, Z.; Zhang, K.; Zhu, Z., N-Heterocycles Extended π-Conjugation Enables Ultrahigh Capacity, Long-Lived, and Fast-Charging Organic Cathodes for Aqueous Zinc Batteries. CCS Chem. 2022, 0 (0), 1-13.

26. Gao, Y.; Li, G.; Wang, F.; Chu, J.; Yu, P.; Wang, B.; Zhan, H.; Song, Z., A high-performance aqueous rechargeable zinc battery based on organic cathode integrating quinone and pyrazine. Energy Storage Mater. 2021, 40, 31-40.

27. Zhao, Q.; Huang, W.; Luo, Z.; Liu, L.; Lu, Y.; Li, Y.; Li, L.; Hu, J.; Ma, H.; Chen, J., High-capacity aqueous zinc batteries using sustainable quinone electrodes. Sci. Adv. 4 (3), eaao1761.

28. Na, M.; Oh, Y.; Byon, H. R., Effects of Zn2+ and H+ Association with Naphthalene Diimide Electrodes for Aqueous Zn-Ion Batteries. Chem. Mater. 2020, 32 (16), 6990-6997.

29. Shi, Y.; Wang, P.; Gao, H.; Jin, W.; Chen, Y.; Huang, Y.; Wu, T.-R.; Wu, D.-Y.; Xu, J.; Cao, J., π-Conjugated N-heterocyclic compound with redox-active quinone and pyrazine moieties as a high-capacity organic cathode for aqueous zinc-ion batteries. Chem. Eng. J. 2023, 461, 141850.

30. Han, C.; Li, H.; Shi, R.; Zhang, T.; Tong, J.; Li, J.; Li, B., Organic quinones towards advanced electrochemical energy storage: recent advances and challenges. J. Mater. Chem. A 2019, 7 (41), 23378-23415.

31. Cui, H.; Ma, L.; Huang, Z.; Chen, Z.; Zhi, C., Organic materials-based cathode for zinc ion battery. SmartMat 2022, 3 (4), 565-581.

32. Tie, Z.; Niu, Z., Design Strategies for High-Performance Aqueous Zn/Organic Batteries. Angew. Chem. Int. Ed. 2020, 59 (48), 21293-21303.

33. Mohamed, M. G.; El-Mahdy, A. F. M.; Kotp, M. G.; Kuo, S.-W., Advances in porous organic polymers: syntheses, structures, and diverse applications. Materials Adv. 2022, 3 (2), 707-733.

34. Kumankuma-Sarpong, J.; Tang, S.; Guo, W.; Fu, Y., Naphthoquinone-Based Composite Cathodes for Aqueous Rechargeable Zinc-Ion Batteries. ACS Appl. Mater. Interfaces 2021, 13 (3), 4084-4092.

35. Khayum M, A.; Ghosh, M.; Vijayakumar, V.; Halder, A.; Nurhuda, M.; Kumar, S.; Addicoat, M.; Kurungot, S.; Banerjee, R., Zinc ion interactions in a two-dimensional covalent organic framework based aqueous zinc ion battery. Chem. Sci. 2019, 10 (38), 8889-8894.

36. Wang, W.; Kale, V. S.; Cao, Z.; Kandambeth, S.; Zhang, W.; Ming, J.; Parvatkar, P. T.; Abou-Hamad, E.; Shekhah, O.; Cavallo, L.; Eddaoudi, M.; Alshareef, H. N., Phenanthroline Covalent Organic Framework Electrodes for High-Performance Zinc-Ion Supercapattery. ACS Energy Lett. 2020, 5 (7), 2256-2264.

37. Wang, W.; Kale, V. S.; Cao, Z.; Lei, Y.; Kandambeth, S.; Zou, G.; Zhu, Y.; Abouhamad, E.; Shekhah, O.; Cavallo, L.; Eddaoudi, M.; Alshareef, H. N., Molecular Engineering of Covalent Organic Framework Cathodes for Enhanced Zinc-Ion Batteries. Adv. Mater. 2021, 33 (39), 2103617.

38. Wang, Y.; Wang, X.; Tang, J.; Tang, W., A quinoxalinophenazinedione covalent triazine framework for boosted high-performance aqueous zinc-ion batteries. J. Mater. Chem. A 2022, 10 (26), 13868-13875.

39. Wang, X.; Tang, J.; Tang, W., Manipulating Polymer Configuration to Accelerate Cation Intercalation Kinetics for High-Performance Aqueous Zinc-Ion Batteries. Adv. Funct. Mater. 2022, 32 (27), 2200517.

40. Wang, X.; Zhou, J.; Li, Z.; Tang, W., N-Heteroaromatic fused-ring cyanides extended as redox polymers for high rate capability aqueous zinc-ion battery. J. Mater. Chem. A 2023, 11 (5), 2412-2418.

41. Ma, D.; Zhao, H.; Cao, F.; Zhao, H.; Li, J.; Wang, L.; Liu, K., A carbonyl-rich covalent organic framework as a high-performance cathode material for aqueous rechargeable zinc-ion batteries. Chem. Sci. 2022, 13 (8), 2385-2390.

42. Lin, Z.; Lin, L.; Zhu, J.; Wu, W.; Yang, X.; Sun, X., An Anti-Aromatic Covalent Organic Framework Cathode with Dual-Redox Centers for Rechargeable Aqueous Zinc Batteries. ACS Appl. Mater. Interfaces 2022, 14 (34), 38689-38695.

43. Zheng, S.; Shi, D.; Yan, D.; Wang, Q.; Sun, T.; Ma, T.; Li, L.; He, D.; Tao, Z.; Chen, J., Orthoquinone–Based Covalent Organic Frameworks with Ordered Channel Structures for Ultrahigh Performance Aqueous Zinc–Organic Batteries. Angew. Chem. Int. Ed. 2022, 61 (12), e202117511.

44. Ye, F.; Liu, Q.; Dong, H.; Guan, K.; Chen, Z.; Ju, N.; Hu, L., Organic Zinc-Ion Battery: Planar, π-Conjugated Quinone-Based Polymer Endows Ultrafast Ion Diffusion Kinetics. Angew. Chem. Int. Ed. 2022, 61 (51), e202214244.

45. Antonietti, M., Introduction to Porous Materials. By Pascal van der Voort, Karen Leus, and Els de Canck. Angew. Chem. Int. Ed. 2020, 59 (33), 13693-13693.

46. Patel, H. A.; Hyun Je, S.; Park, J.; Chen, D. P.; Jung, Y.; Yavuz, C. T.; Coskun, A., Unprecedented high-temperature CO2 selectivity in N2-phobic nanoporous covalent organic polymers. Nat. Commun. 2013, 4 (1), 1357.

47. Li, Z.; Yang, Y.-W., Macrocycle-Based Porous Organic Polymers for Separation, Sensing, and Catalysis. Adv. Mater. 2022, 34 (6), 2107401.

48. Xu, H.; Gao, J.; Jiang, D., Stable, crystalline, porous, covalent organic frameworks as a platform for chiral organocatalysts. Nature Chemistry 2015, 7 (11), 905-912.

49. Guo, L.; Cao, D., Color tunable porous organic polymer luminescent probes for selective sensing of metal ions and nitroaromatic explosives. Journal of Materials Chemistry C 2015, 3 (33), 8490-8494.

50. Singh, N.; Son, S.; An, J.; Kim, I.; Choi, M.; Kong, N.; Tao, W.; Kim, J. S., Nanoscale porous organic polymers for drug delivery and advanced cancer theranostics. Chem. Soc. Rev. 2021, 50 (23), 12883-12896.

51. Ritchie, L. K.; Trewin, A.; Reguera-Galan, A.; Hasell, T.; Cooper, A. I., Synthesis of COF-5 using microwave irradiation and conventional solvothermal routes. Microporous Mesoporous Mater. 2010, 132 (1), 132-136.

52. Biswal, B. P.; Chandra, S.; Kandambeth, S.; Lukose, B.; Heine, T.; Banerjee, R., Mechanochemical Synthesis of Chemically Stable Isoreticular Covalent Organic Frameworks. J. Am. Chem. Soc. 2013, 135 (14), 5328-5331.

53. Fang, Q.; Zhuang, Z.; Gu, S.; Kaspar, R. B.; Zheng, J.; Wang, J.; Qiu, S.; Yan, Y., Designed synthesis of large-pore crystalline polyimide covalent organic frameworks. Nat. Commun. 2014, 5 (1), 4503.

54. Meng, Y.; Luo, Y.; Shi, J.-L.; Ding, H.; Lang, X.; Chen, W.; Zheng, A.; Sun, J.; Wang, C., 2D and 3D Porphyrinic Covalent Organic Frameworks: The Influence of Dimensionality on Functionality. Angew. Chem. Int. Ed. 2020, 59 (9), 3624-3629.

55. Bourda, L.; Krishnaraj, C.; Van Der Voort, P.; Van Hecke, K., Conquering the crystallinity conundrum: efforts to increase quality of covalent organic frameworks. Materials Adv. 2021, 2 (9), 2811-2845.

56. Buyukcakir, O.; Je, S. H.; Talapaneni, S. N.; Kim, D.; Coskun, A., Charged Covalent Triazine Frameworks for CO2 Capture and Conversion. ACS Appl. Mater. Interfaces 2017, 9 (8), 7209-7216.

57. Jiang, J.-X.; Su, F.; Trewin, A.; Wood, C. D.; Niu, H.; Jones, J. T. A.; Khimyak, Y. Z.; Cooper, A. I., Synthetic Control of the Pore Dimension and Surface Area in Conjugated Microporous Polymer and Copolymer Networks. J. Am. Chem. Soc. 2008, 130 (24), 7710-7720.

58. Schmidt, J.; Werner, M.; Thomas, A., Conjugated Microporous Polymer Networks via Yamamoto Polymerization. Macromolecules 2009, 42 (13), 4426-4429.

59. Ben, T.; Ren, H.; Ma, S.; Cao, D.; Lan, J.; Jing, X.; Wang, W.; Xu, J.; Deng, F.; Simmons, J. M.; Qiu, S.; Zhu, G., Targeted Synthesis of a Porous Aromatic Framework with High Stability and Exceptionally High Surface Area. Angew. Chem. Int. Ed. 2009, 48 (50), 9457-9460.

60. Li, B.; Gong, R.; Wang, W.; Huang, X.; Zhang, W.; Li, H.; Hu, C.; Tan, B., A New Strategy to Microporous Polymers: Knitting Rigid Aromatic Building Blocks by External Cross-Linker. Macromolecules 2011, 44 (8), 2410-2414.

61. Luo, Y.; Li, B.; Wang, W.; Wu, K.; Tan, B., Hypercrosslinked Aromatic Heterocyclic Microporous Polymers: A New Class of Highly Selective CO2 Capturing Materials. Adv. Mater. 2012, 24 (42), 5703-5707.

62. Fritz, P. W.; Chen, T.; Ashirov, T.; Nguyen, A.-D.; Dincă, M.; Coskun, A., Fully Conjugated Tetraoxa[8]circulene-Based Porous Semiconducting Polymers. Angew. Chem. Int. Ed. 2022, 61 (17), e202116527.

63. Wang, J.; Polleux, J.; Lim, J.; Dunn, B., Pseudocapacitive Contributions to Electrochemical Energy Storage in TiO2 (Anatase) Nanoparticles. J. Phys. Chem. C 2007, 111 (40), 14925-14931.

APPENDIX A

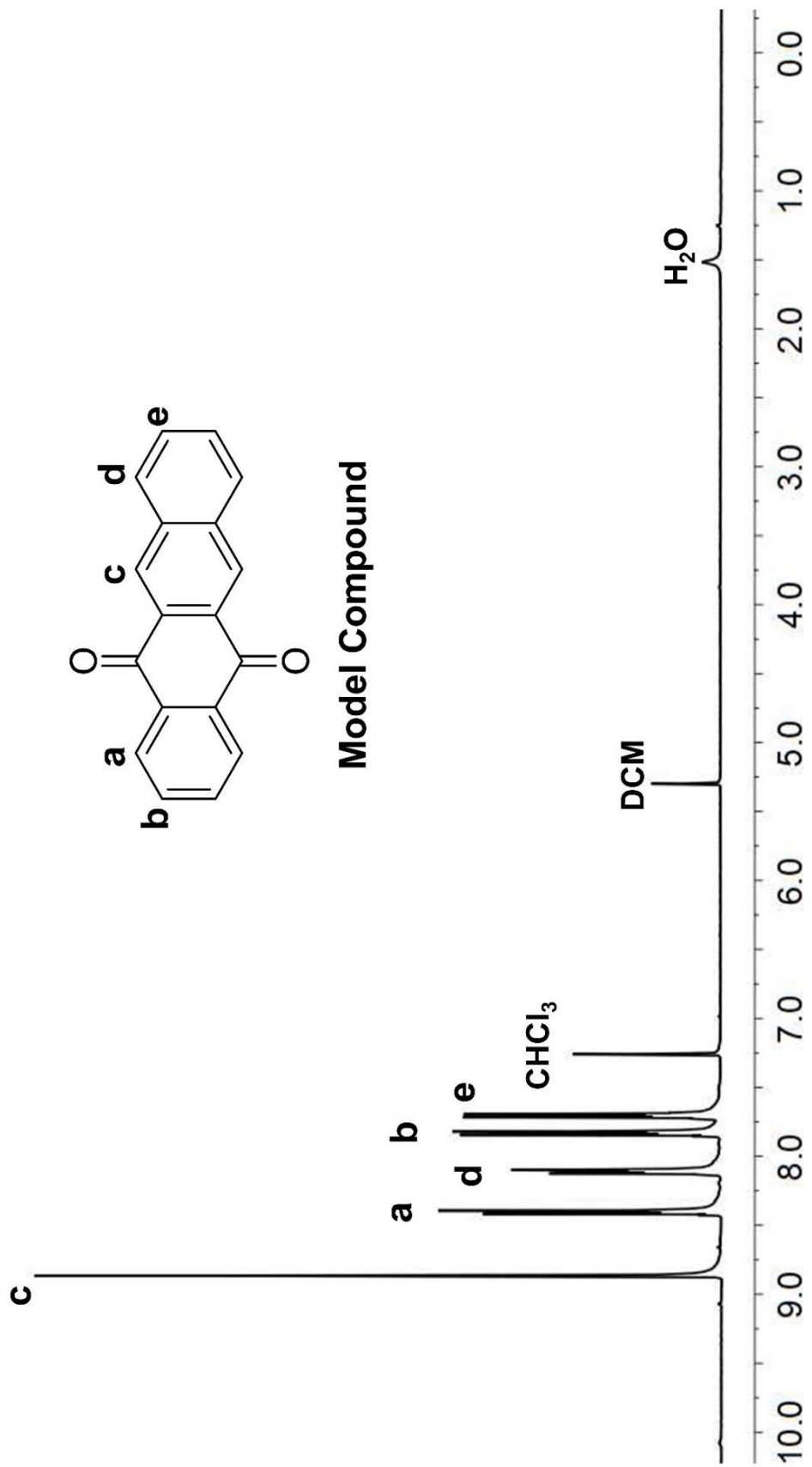# ^{1}H-NMR AND ^{13}C-NMR SPECTRA OF COMPOUND

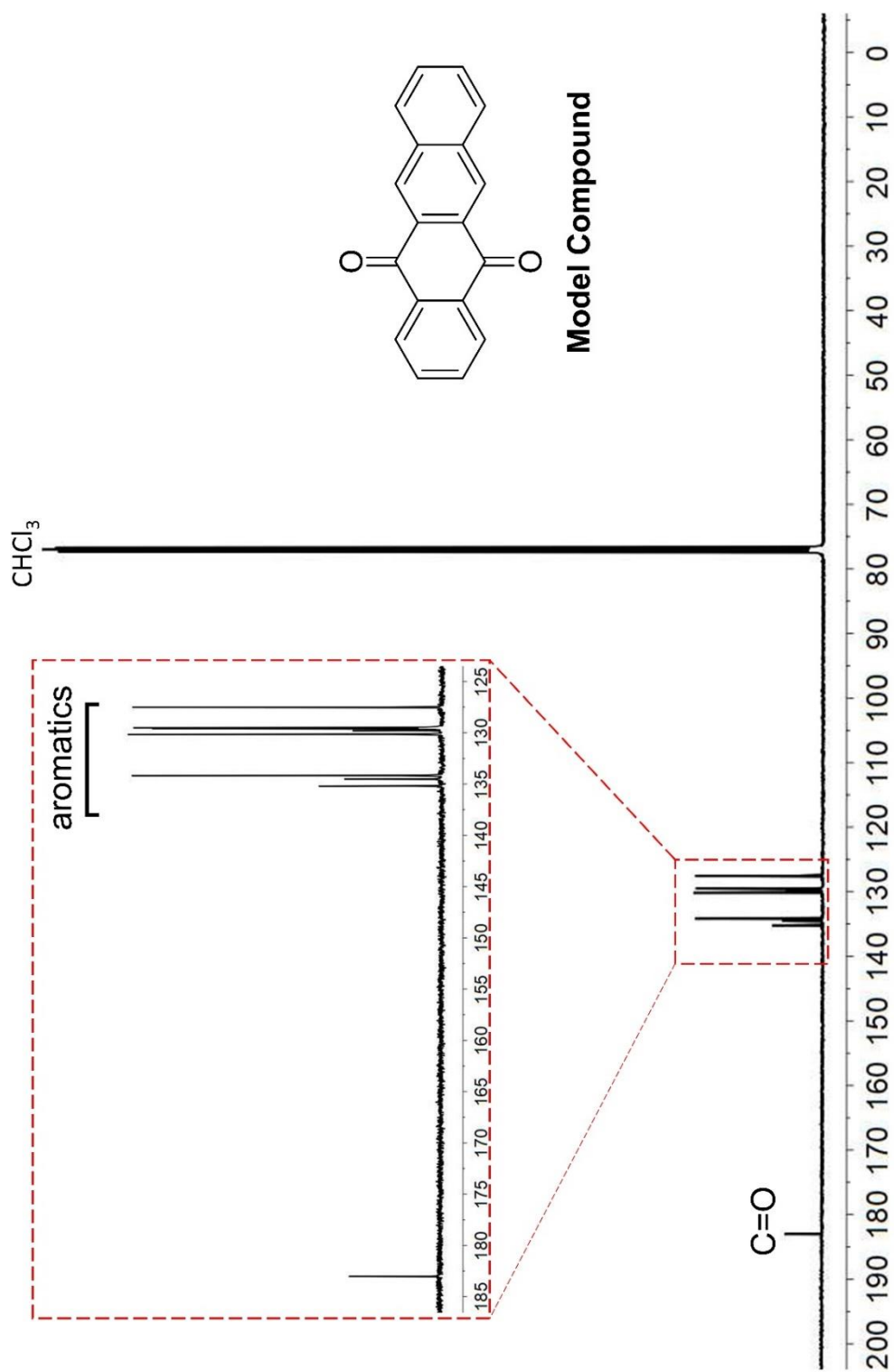Figure A1. ^{1}H-NMR spectrum of model compound.

Figure A2. ^{13}C-NMR spectrum of model compound.

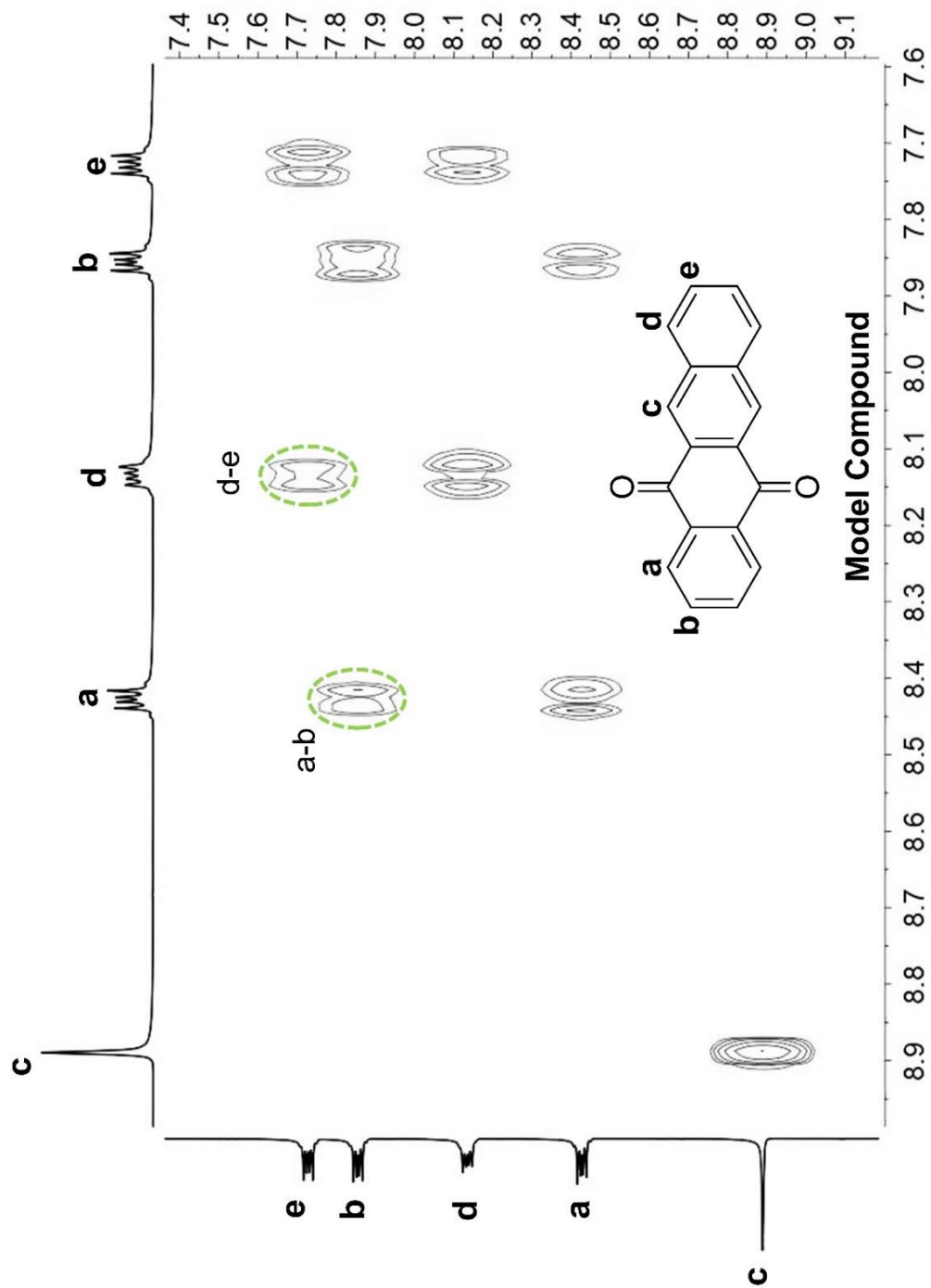Figure A3. ^{1}H-^{1}H COSY spectrum of model compound.

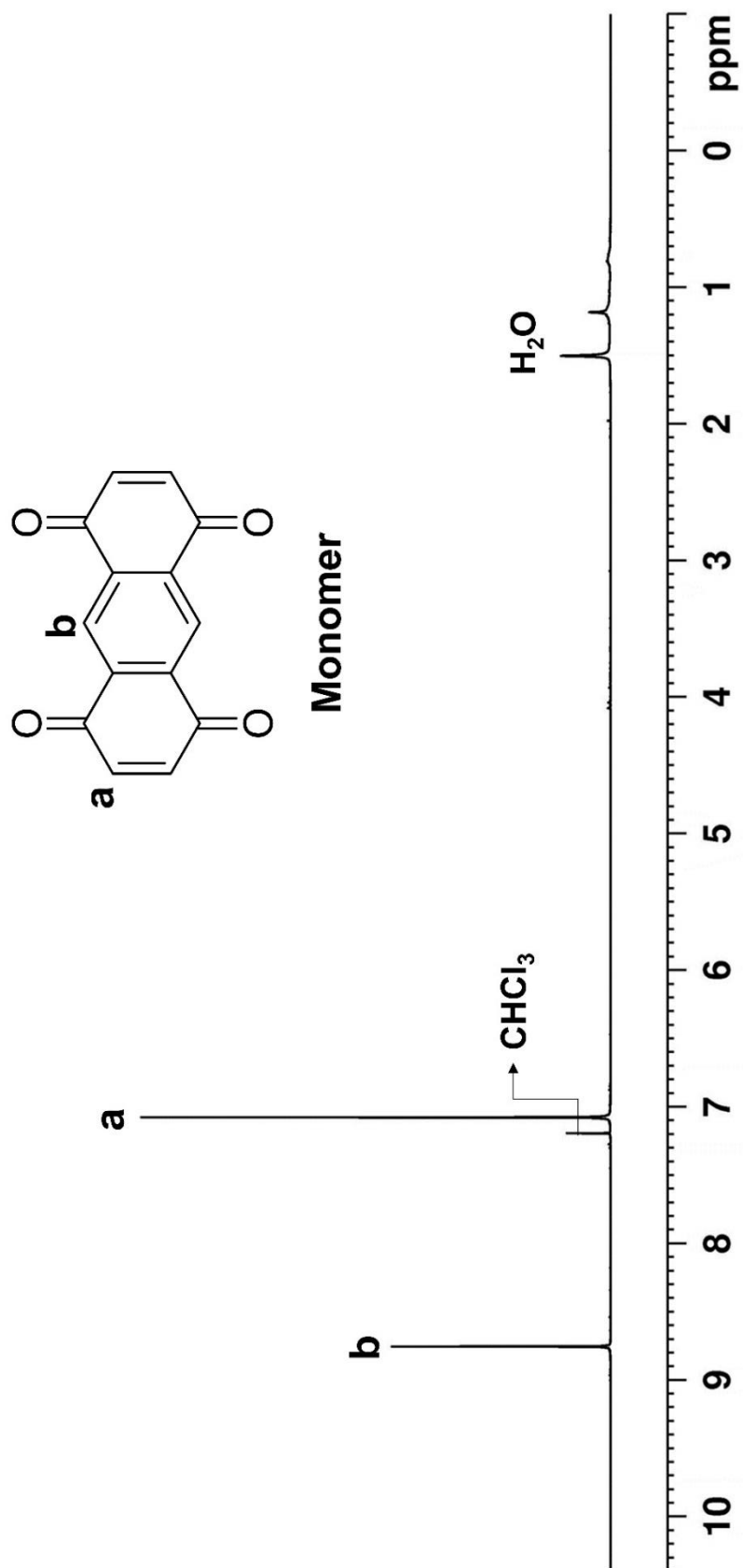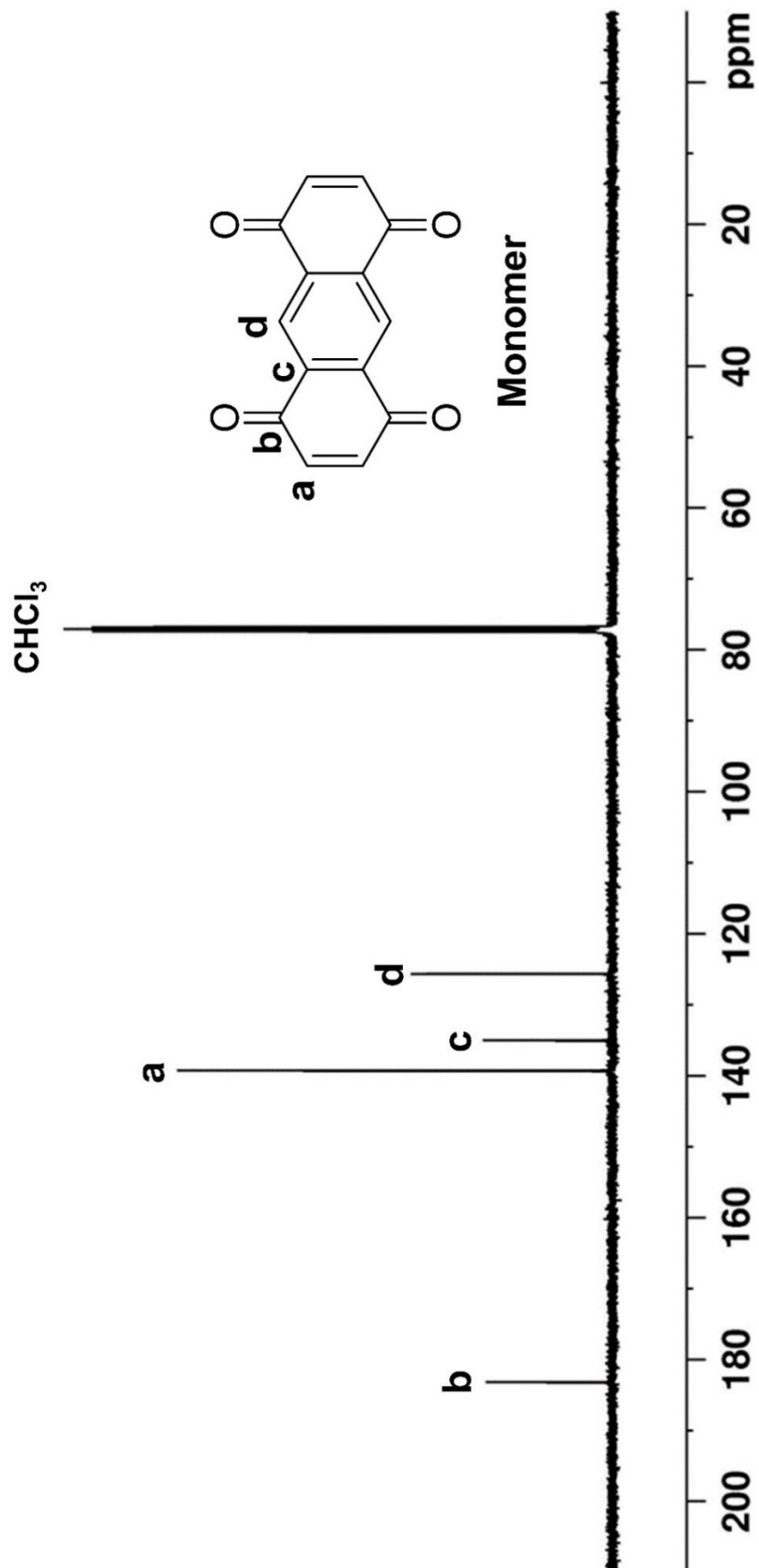Figure A4. ^{1}H-NMR spectrum of 1,4,5,8-Anthracenetetrone (monomer).

Figure A5. ^{13}C-NMR spectrum of 1,4,5,8-Anthracenetetrone (monomer).